



Less Than 1% of Core-collapse Supernovae in the Local Universe Occur in Elliptical Galaxies

I. Irani¹, S. J. Prentice², S. Schulze^{1,3}, A. Gal-Yam¹, Jacob Teffs⁴, Paolo Mazzali^{4,5}, J. Sollerman⁶, E. P. Gonzalez^{7,8}, K. Taggart⁹, Kishalay De¹⁰, Christoffer Fremling¹¹, Daniel A. Perley⁴, Nora L. Strotjohann¹, Mansi M. Kasliwal¹¹, A. Howell^{7,8}, S. Dhawan^{3,12}, Anastasios Tzanidakis¹⁰, Daichi Hiramatsu^{7,8}, Erik C. Kool⁶, J. P. Anderson¹³, T. E. Müller-Bravo¹⁴, Richard Dekany¹⁵, Mariusz Gromadzki¹⁶, Roberta Carini¹⁷, L. Galbany¹⁸, Andrew J. Drake¹¹, Jamison Burke^{7,8}, Craig Pellegrino^{7,8}, Massimo Della Valle^{19,20,21}, Michael S. Medford^{22,23}, Ben Rusholme²⁴, D. R. Young²⁵, Claudia P. Gutiérrez^{26,27}, Cosimo Inserra²⁸, Rafia Omer²⁹, David L. Shupe²⁴, T.-W. Chen⁶, Kyung Min Shin³⁰, Ofer Yaron¹, Curtis McCully⁷, Matt Nicholl³¹, and Reed Riddle¹⁵

¹ Department of Particle Physics and Astrophysics, Weizmann Institute of Science, 234 Herzl St., 7610001 Rehovot, Israel; idoirani@gmail.com

² School of Physics, Trinity College Dublin, The University of Dublin, Dublin 2, Ireland

³ Department of Physics, The Oskar Klein Center, Stockholm University, AlbaNova, SE-10691 Stockholm, Sweden

⁴ Astrophysics Research Institute, Liverpool John Moores University, IC2 Liverpool Science Park, 146 Brownlow Hill, Liverpool L3 5RF, UK

⁵ Max-Planck Institut für Astrophysik, Karl-Schwarzschild-Str. 1, D-85741 Garching, Germany

⁶ Department of Astronomy, The Oskar Klein Center, Stockholm University, AlbaNova, SE-10691 Stockholm, Sweden

⁷ Las Cumbres Observatory, 6740 Cortona Dr., Suite 102, Goleta, CA, 93117, USA

⁸ Department of Physics, University of California, Santa Barbara, Santa Barbara, CA, 93106, USA

⁹ Department of Astronomy and Astrophysics, University of California, Santa Cruz, CA 95064, USA

¹⁰ Cahill Center for Astrophysics, California Institute of Technology, 1200 E. California Blvd., Pasadena, CA 91125, USA

¹¹ Division of Physics, Mathematics and Astronomy, California Institute of Technology, Pasadena, CA 91125, USA

¹² Kavli Institute for Cosmology, University of Cambridge, Madingley Road, Cambridge CB3 0HA, UK

¹³ European Southern Observatory, Alonso de Córdova 3107, Casilla 19, Santiago, Chile

¹⁴ School of Physics and Astronomy, University of Southampton, Southampton, Hampshire, SO17 1BJ, UK

¹⁵ Caltech Optical Observatories, California Institute of Technology, Pasadena, CA 91125, USA

¹⁶ Astronomical Observatory, University of Warsaw, Al. Ujazdowskie 4, 00-478 Warszawa, Poland

¹⁷ INAF-Osservatorio Astronomico di Roma, Via Frascati 33, I-00040 Monte Porzio Catone (RM), Italy

¹⁸ Institute of Space Sciences (ICE, CSIC), Campus UAB, Carrer de Can Magrans, s/n, E-08193 Barcelona, Spain

¹⁹ INAF-Capodimonte Astronomical Observatory, Salita Moiariello 16, 80131 Naples, Italy

²⁰ INFN Naples, Naples I-80126, Italy

²¹ ICRANet, Piazza della Repubblica 10, I-65122 Pescara, Italy

²² Department of Astronomy, University of California, Berkeley, Berkeley, CA 94720, USA

²³ Lawrence Berkeley National Laboratory, 1 Cyclotron Rd., Berkeley, CA 94720, USA

²⁴ IPAC, California Institute of Technology, 1200 E. California Blvd., Pasadena, CA 91125, USA

²⁵ Astrophysics Research Centre, School of Mathematics and Physics, Queen's University Belfast, Belfast BT7 1NN, UK

²⁶ Finnish Centre for Astronomy with ESO (FINCA), FI-20014 University of Turku, Finland

²⁷ Tuorla Observatory, Department of Physics and Astronomy, FI-20014 University of Turku, Finland

²⁸ School of Physics & Astronomy, Cardiff University, Queens Buildings, The Parade, Cardiff, CF24 3AA, UK

²⁹ School of Physics and Astronomy, University of Minnesota, 116 Church St. SE, Minneapolis MN 55455, USA

³⁰ California Institute of Technology, Pasadena, CA 91125, USA

³¹ Birmingham Institute for Gravitational Wave Astronomy and School of Physics and Astronomy, University of Birmingham, Birmingham B15 2TT, UK

Received 2021 October 5; revised 2021 December 12; accepted 2021 December 13; published 2022 March 2

Abstract

We present observations of three core-collapse supernovae (CCSNe) in elliptical hosts, detected by the Zwicky Transient Facility Bright Transient Survey (BTS). SN 2019ape is a SN Ic that exploded in the main body of a typical elliptical galaxy. Its properties are consistent with an explosion of a regular SN Ic progenitor. A secondary *g*-band light-curve peak could indicate interaction of the ejecta with circumstellar material (CSM). An H α -emitting source at the explosion site suggests a residual local star formation origin. SN 2018fsh and SN 2020uik are SNe II which exploded in the outskirts of elliptical galaxies. SN 2020uik shows typical spectra for SNe II, while SN 2018fsh shows a boxy nebular H α profile, a signature of CSM interaction. We combine these 3 SNe with 7 events from the literature and analyze their hosts as a sample. We present multi-wavelength photometry of the hosts, and compare this to archival photometry of all BTS hosts. Using the spectroscopically complete BTS, we conclude that $0.3\%_{-0.1}^{+0.3}$ of all CCSNe occur in elliptical galaxies. We derive star formation rates and stellar masses for the host galaxies and compare them to the properties of other SN hosts. We show that CCSNe in ellipticals have larger physical separations from their hosts compared to SNe Ia in elliptical galaxies, and discuss implications for star-forming activity in elliptical galaxies.

Unified Astronomy Thesaurus concepts: Core-collapse supernovae (304); Early-type galaxies (429); Star formation (1569)

Supporting material: machine-readable table



Original content from this work may be used under the terms of the [Creative Commons Attribution 4.0 licence](https://creativecommons.org/licenses/by/4.0/). Any further distribution of this work must maintain attribution to the author(s) and the title of the work, journal citation and DOI.

1. Introduction

Core-collapse supernovae (CCSNe) are widely considered to be the terminal explosion of massive ($>8 M_{\odot}$) stars. Except for SNe Ia and Ca-Rich SNe Ib, which are likely thermonuclear explosions of white dwarf stars, all other major SN types are currently thought to have a massive star origin (Gal-Yam 2017 and references therein). Specifically, all hydrogen-rich SNe (SNe II), hydrogen-poor and silicon-poor SNe (SNe Ib/c and SNe Ibn), and superluminous SNe (SLSN) are thought to have a massive star origin. The progenitors of most SNe II are thought to be red supergiants (RSG), as confirmed by direct progenitor detections in deep pre-explosion images (for reviews, see Smartt 2015; Van Dyk 2017 and references therein). The progenitors of SNe Ic have not yet been solidly detected (Eldridge et al. 2013; Smartt 2015, but c.f. Van Dyk et al. 2018). They are thought to be either massive, single Wolf-Rayet (WR) stars (e.g., Taddia et al. 2019), or massive stars whose hydrogen-rich envelope has been stripped in a binary interaction (Eldridge et al. 2013). As expected, SNe Ic have been found exclusively in star-forming environments. Similarly, other CCSN types are rarely found outside of such environments (e.g., Hakobyan et al. 2012). Suh et al. (2011) investigated previous claims of CCSNe in early-type (i.e., elliptical and lenticular) host galaxies, but found that these were either the result of an erroneous SN classification, or that the host galaxies had a systematically bluer ultraviolet (UV)—optical color than the early-type hosts of SNe Ia ($\text{NUV} - r_{\text{PS1}} \sim 3$ mag compared to $\text{NUV} - r_{\text{PS1}} \sim 5.4$ mag, respectively). Recently, Sedgwick et al. (2021) reported 36 CCSNe occurring in elliptical galaxies from a sample of 421 photometrically classified CCSNe from the SDSS-II Supernova Survey (Sako et al. 2018) and argue that elliptical galaxies account for $\sim 11\%$ of the cosmic star formation budget. Kaviraj (2014) estimated, based on the Sloan Digital Sky Survey (SDSS; York et al. 2000) stripe 82 data, that the contribution of early-type galaxies to the cosmic star formation budget is 14%.

A few cases of CCSNe in the outskirts of non-star-forming elliptical galaxies have been reported. SN 2016hil was a SN II found at a relatively large offset of 26 kpc from the center of a massive elliptical galaxy (Irani et al. 2019). The SN Ibn PS1-12sk was found at a similar offset from a massive elliptical galaxy (Sanders et al. 2013). In both cases, the large offset from the massive nearby elliptical galaxy might indicate that the association is spurious, although deep observations of the SN site using the Hubble Space Telescope (HST) and Keck argue against an underlying faint host galaxy (Hosseinzadeh et al. 2019; Irani et al. 2019).

Hubble first classified galaxies using a “tuning fork” scheme (Hubble 1926), using the presence of spiral and bar features. This scheme was later improved (e.g., by de Vaucouleurs 1959; Sandage 1961) to include finer morphological features. Galaxy morphology is broadly categorized into bulge-dominated “red and dead” early-type galaxies and blue star-forming late-type galaxies. While the colors, morphologies, and star formation of galaxies are tightly correlated, they do not map exactly onto each other (Trager et al. 2000; Strateva et al. 2001; De Lucia et al. 2006; Buta 2011). The observed bimodality in galaxy colors and star formation properties requires a physical mechanism to quench star formation in massive evolved galaxies; a topic of ongoing research (e.g., Gabor et al. 2010; Man & Belli 2018).

While generally considered passive galaxies, the low-level star formation still ongoing in some early-type galaxies is a topic of

ongoing research. Kaviraj et al. (2008) found that up to $\sim 30\%$ of early-type galaxies might have undergone recent episodes of star formation, leading to bluer UV–optical colors. Hernández & Bruzual (2009) further suggest that the blue colors of early-type galaxies with $4 < \text{NUV} - r_{\text{PS1}} < 5.4$ mag could be explained by a recent low-level star-forming episode or by the presence of extreme horizontal branch (EHB) stars. Petty et al. (2013) also suggested EHB stars are the source of the blue UV–optical colors of UV excess early-type galaxies. Salim et al. (2012) studied a sample of early-type galaxies from the SDSS survey with a strong UV excess and found structured UV morphology in 93% of their sample. In 75% of the cases, the star formation extended to offsets of 25–75 kpc, indicative of galaxy-scale inside-out growth, fueled by accretion of gas from the intergalactic medium (IGM). Such growth is found to occur for massive galaxies (Sánchez-Blázquez et al. 2007; Pérez et al. 2013). The rest of their sample is characterized by patchy and centered (5–15 kpc) star formation. By contrast, Gomes et al. (2016) found star-forming lanes in 3 nearby early-type galaxies, documenting the still ongoing star formation in these galaxies. Assuming the ongoing star formation in elliptical galaxies is similar to star formation in spirals, a population of SNe is expected to explode in these environments.

New transient surveys such as the Zwicky Transient Facility (ZTF; Bellm et al. 2019; Graham et al. 2019; Dekany et al. 2020), the Asteroid Terrestrial Last Alert System (ATLAS; Tonry et al. 2018), the Panoramic Survey Telescope and Rapid Response System 1 (PS1; Chambers et al. 2016), and the All Sky Automated Survey for Supernovae (ASAS-SN; Shappee et al. 2014), monitor the entire night sky with a high cadence and to unprecedented depths and discover thousands of SNe in the process. This allows SNe to be used as probes to trace star formation in elliptical galaxies where star formation was thought to have ceased. The ZTF Bright Transient Survey (BTS; Fremling et al. 2020; Perley et al. 2020) is the largest untargeted spectroscopically complete SN survey to date. It classifies 93% of all SNe with peak magnitudes $m_{\text{peak}} < 18.5$ mag and 75% of all SNe with $m_{\text{peak}} < 19$ mag. This sample allows for a systematic study of residual CCSN populations in low-redshift environments.

In this paper, we used the BTS to conduct a search for spectroscopically confirmed CCSNe in elliptical host galaxies. We present observations of three such SNe. We combine these events with a sample of literature objects, analyze the SN properties, and characterize their host environments. This paper is organized as follows. In Section 2 we describe our sample selection and the comparison samples. In Section 3 we present the spectroscopic and photometric observations of the SNe and their hosts. In Section 4 we characterize the transients and their host galaxies. We discuss the implications of these results and present our conclusions in Section 5. Throughout this paper we assume $H_0 = 73 \text{ km s}^{-1} \text{ Mpc}^{-1}$ and a Λ CDM cosmology with $\Omega_m = 0.27$ and $\Omega_{\Lambda} = 0.73$ (Wilkinson Microwave Anisotropy Probe 3 yr results; Spergel et al. 2007). All magnitudes are reported in the AB system and are corrected for line-of-sight reddening based on Schlafly & Finkbeiner (2011); see Section 2.5.

2. Sample

2.1. Candidate Selection Process

As of 2020 December 30, the BTS sample contains 4018 spectroscopically classified SNe. Of these, we select SNe satisfying the following criteria:

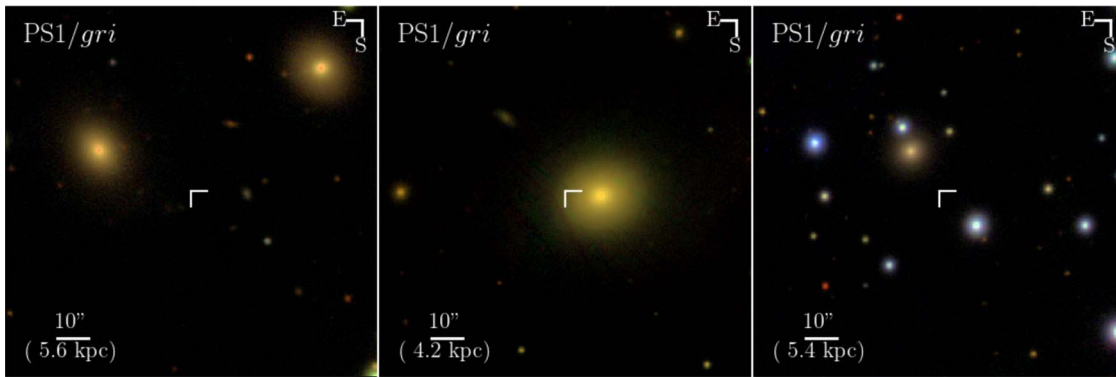


Figure 1. The host galaxies of (from left to right) SN 2018fsh, SN 2019ape, and SN 2020uik, constructed from PS1 stacks in the *gri* bands. The location of the SN is marked with white crosshairs. The angular scale is provided in the lower left corner of each panel.

1. The redshift is $0.015 < z < 0.1$. The lower bound is meant to avoid shredding of nearby galaxies into multiple sources in galaxy catalogs and the upper bound is due to the reduced completeness of galaxy redshift catalogs (Fremling et al. 2020), required to ensure the SN and the galaxy are indeed associated.
2. The likely host galaxies of the ZTF BTS SNe are continuously identified in the BTS sample explorer³² (Perley et al. 2020). This is done by an automatic cross matching of the SN positions with the nearest galaxies in the Pan-STARRS (PS1; Chambers et al. 2016) or SDSS (Alam et al. 2015) photometric catalogs. Host-galaxy matching is complete out to an offset of $< 90''$ and < 30 kpc (projected distance) and employs a criterion to distinguish between multiple host-galaxy associations. We only select SNe that are associated with a host galaxy in this way.

Of the 4018 SNe in the sample, 3855 had a redshift in the required range. Among those, we could identify the most likely host galaxy of 3330 SNe. We cross match these host galaxies with the Galaxy Evolution Explorer (GALEX) Data Release (DR) 8/9 (Martin et al. 2005) and the ALLWISE (Cutri et al. 2021) catalogs and obtain the FUV (1542 Å), NUV (2274 Å) and W1–W4 [33,500 Å–220,000 Å] IR photometry. We correct the results for Galactic reddening using the maps of Schlafly & Finkbeiner (2011). Queries were performed from the VizieR Catalog (Ochsenbein et al. 2000) using *astroquery* (Ginsburg 2019). We use the host photometry to define a sample of CCSNe with early-type hosts. These are defined here as:

1. Galaxies with $W2 - W3 < 0.5$ mag and $NUV - r_{PS1} > 3$ mag, if both the $W2 - W3$ color and the $NUV - r_{PS1}$ colors are available.
2. Or galaxies with $W2 - W3 < 0.3$, if only the $W2 - W3$ color is available.

This definition is satisfied by 75% of elliptical galaxies in the Galaxy Zoo (Lintott et al. 2011) sample. It is chosen so that it includes all regions in the color–color parameter space that have a higher number of ellipticals compared to spirals, calculated in 0.5 mag bins.

Next, we search for any SN not classified as an SN Ia, and examine the host morphology visually. To be considered a CCSN in an elliptical host, we require:

1. Independent and consistent spectroscopic redshift measurements of both the SN and the host galaxy from publicly available catalogs.
2. Visual confirmation of the red color and absence of a bar, spiral arms, or a disk structure in the deepest available images.
3. Once aperture-matched photometry and source deblending is performed, the host galaxy still occupies our double-color region for elliptical galaxies.
4. Confirmation of a CCSN classification: SN classifications in the BTS (Fremling et al. 2020) are made using both human inspection and using SuperNova IDentification (SNID; Blondin & Tonry 2007), and are thus generally reliable. However, since CCSNe generally avoid elliptical galaxies, we take special care to avoid misclassified SNe Ia and require verification of the SN type through a visual inspection of the spectrum and by fitting the spectra using a python adaptation of Superfit (Howell et al. 2005) with an updated spectrum template bank (S. Goldwasser et al., in preparation).

Twenty-one CCSNe pass our color criteria, of which only 4 SN hosts emerged as having elliptical morphology—SN 2020uik (SN II), SN 2018fsh (SN II), SN 2019ape (SN Ic) and SN 2019cmv (SLSN-II). While SN 2019cmv passes our sample criteria, we exclude it due to the combination of having a high offset from the nearby elliptical galaxy, and the shallow limits on an underlying host at the SN site. At the distance of SN 2019cmv, we cannot rule out the presence of a faint, underlying host with a brightness of ≥ 14 mag. Such low-mass hosts have been observed for several SLSNe (Perley et al. 2016; Schulze et al. 2018), and are the most likely explanation for the unusual location of SN 2019cmv. SN 2020oce, classified as a SN Ic in the BTS, also passes our sample criteria, but we find that it is fit well by spectra of 91bg-like SNe Ia, and so exclude it from our sample. In Figure 1 we show PS1 image cutouts of the three CCSN host galaxies from the BTS matching our criteria. The images are constructed using the method described in Lupton et al. (2004).

The data points in the left panel of Figure 2 show the UV–optical and mid-infrared (MIR) colors of CCSN hosts compared to the colors of elliptical and spiral galaxies from the Galaxy Zoo catalog (Lintott et al. 2011). In this plot, a good separation is achieved between the colors of elliptical and spiral galaxies. In the right panel of Figure 2 we show the same color–color plot for the host galaxies of SNe Ia. As expected, the vast majority of CCSNe occur in the region occupied by

³² <https://sites.astro.caltech.edu/ztf/bts/explorer.php>

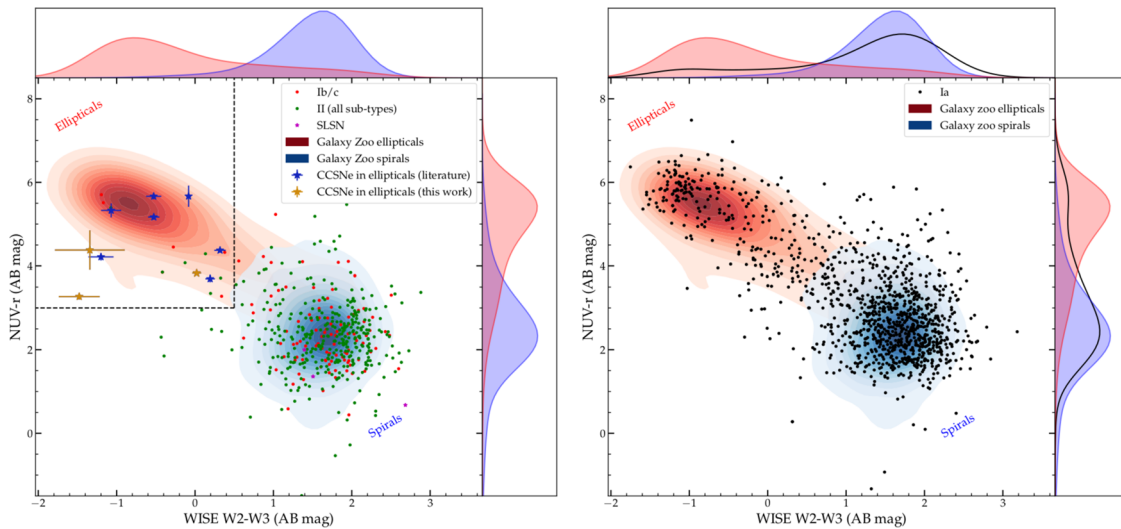


Figure 2. Left: color–color diagram for all CCSNe hosts with full color information. Each data point represents the colors of the host galaxy of an SN. The black dashed lines indicate the region defining our color criterion for elliptical galaxies. SNe whose hosts passed our criteria as elliptical galaxies are marked with a yellow star (this work) or a blue star (literature sample), using the host photometry reported in this work. All BTS CCSN hosts are marked with dots color-coded based on the SN type as indicated in the legend. The red and blue shaded regions are the 2d smoothed distributions of Galaxy Zoo ellipticals and spirals. These also appear as a 1D color kernel density estimate on the top and right panels. Right: similar to the previous plot, but for the hosts of SNe Ia.

spirals. In Figure 3 we show the mean observed colors of spirals and ellipticals from the Galaxy Zoo catalog normalized to the W2 band and compare them with the colors of elliptical host galaxies of CCSNe. As this figure shows, the most significant difference between the spectral energy distribution (SED) of spiral and elliptical galaxies is seen in the UV and in the MIR. The elliptical host galaxies of CCSNe have SEDs similar to galaxy zoo ellipticals.

2.2. Literature Sample

In addition to the objects presented in this paper, we compile a sample of CCSNe in elliptical galaxies from the literature. We apply the criteria in Section 2.1 to the CCSN sample (Schulze et al. 2021) from the Palomar Transient Factory (PTF; Law et al. 2009) and the intermediate Palomar Transient Factory (iPTF; Kulkarni 2013), and to published CCSNe from Suh et al. (2011), Hakobyan et al. (2008), Graham et al. (2012), and Sanders et al. (2013). Our findings generally agree with the conclusions of these papers—that most CCSNe near elliptical galaxies occurred in either misclassified spirals or star-forming ellipticals. A small minority of the SNe analyzed in these papers do pass our criteria, and we combine these with our BTS objects to form a combined sample. We further require that objects in our sample have public spectra, so that the classification can be confirmed. In total, our combined sample includes 10 SNe, listed in Table 1, along with their classifications and estimated peak luminosities. We note that the host of the Type II SN Abell 399 11 19 0 (Graham et al. 2012) did not pass our sample inclusion criteria since it is not detected in both the NUV and W3 bands. However, the available limits ($W2 - W3 < 0.06$ mag, $NUV - r_{PS1} > 4.5$ mag), along with the galaxy morphology, indicate this host is also an elliptical galaxy.

2.3. Comparison Samples

Throughout this work, we use several SN and galaxy samples for comparison. These are:

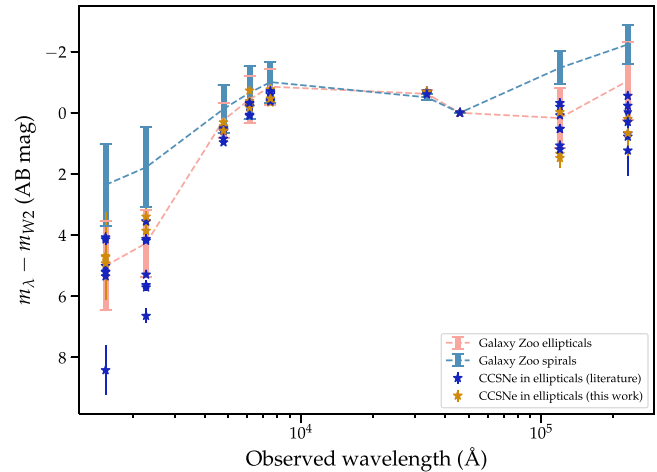


Figure 3. The observed host colors relative to the W2 band for Galaxy Zoo spirals (cyan) and Galaxy Zoo ellipticals (pink). CCSN host galaxies that passed our criteria as true elliptical galaxies are marked with a yellow star (this work) or a blue star (literature sample). The error bars represent the standard deviation of the Galaxy Zoo sample or the measurement error for individual SNe.

1. BTS CCSNe: we selected all BTS SNe classified as CCSNe that occurred in host galaxies with measured WISE $W2 - W3$ and UV–optical colors. This sample consists of 478 objects, of which 465 fall outside of the region that we associate with elliptical galaxies in Figure 2.
2. SNe Ia elliptical galaxies: we selected all BTS SNe (Perley et al. 2020) classified as SNe Ia that occurred in host galaxies with both $W2 - W3 < 0.5$ mag and $NUV - r_{PS1} > 3$ mag. This sample contains 240 objects.
3. Galaxy Zoo (Lintott et al. 2011) galaxies: we randomly selected 50,000 galaxies from the Galaxy Zoo sample that have morphological classifications and with a redshift in the range $0.015 < z < 0.05$. Of these galaxies, 1309 (10265) were classified as elliptical (spiral). Queries were performed using `CasJobs` (OMullane et al. 2005). We

Table 1
Sample of CCSNe with Elliptical Hosts Analyzed in This Work

SN	R.A. (J2000)	Decl. (J2000)	Redshift	Projected Offset (kpc)	Peak M_r (AB mag) ^{a,b}	SN Type	Reference
SN2003ky	179.52625	47.33319	0.047	8.3	-19.3	II	Armstrong (2003)
SN2006ee	29.8975	14.00544	0.015	4.3	-16.64	II	Puckett et al. (2006)
SN2006gy	49.36275	41.40542	0.019	1.1	-20.2	IIn	Ofek et al. (2007); Smith et al. (2007)
PTF10gqf	225.96897	55.62717	0.045	29.0	-16.5	II	Schulze et al. (2021)
PS1-12sk	131.22858	42.97136	0.054	32.9	-19.2	Ibn	Sanders et al. (2013)
SN2016hil	17.603106	14.204318	0.061	26.4	-17.0	II	Irani et al. (2019)
PTF16pq	139.39429	18.95197	0.028	4.0	-16.1	II	Schulze et al. (2021)
SN2018fsh	127.73595	39.83588	0.029	22.8	-18.2	II	This work
SN2019ape	162.92728	18.4813	0.020	4.8	-16.83	Ic	This work
SN2020uik	120.47579	-6.76099	0.028	8.6	-17.22	II	This work

Notes.

^a All measurements are taken from the Open Supernova Catalog (Guillochon et al. 2017) or from cited references.

^b Observed r -band magnitudes were adopted when available. Otherwise, an average between R and V bands was adopted. If no color information was available, we adopt the peak magnitude in the observed band. Magnitudes were corrected for Galactic reddening.

note that Lintott et al. (2011) use a broad categorization of galaxies into ellipticals and spirals. The elliptical group includes both elliptical (E) and lenticular (S0) galaxies.

2.4. SN Discovery and Classification

2.4.1. SN 2018fsh

SN 2018fsh was detected in the ZTF alert stream on UT 2018 August 31.52 (JD 2458362.02) at J2000 coordinates of $\alpha = 08^{\text{h}}30^{\text{m}}56^{\text{s}}.6$, $\delta = +39^{\circ}50'09''.2$ at a brightness of $r = 19.0$ mag (Fremling 2018). Based on a spectrum obtained on UT 2018 September 17.56 (JD 2458379.06) the transient was classified as a SN II (Fremling et al. 2018) at a redshift of $z = 0.029$. This redshift is consistent with the value ($z = 0.029084$) listed in the NASA Extragalactic Database (NED)³³ for MCG +07-18-013, a red galaxy offset by $38''.6$ from the SN location. The host redshift corresponds to a distance of 122 ± 9 Mpc corrected for Virgo, Shapley, and Great attractor infall (Mould et al. 2000, via NED). ZTF did not observe the field in the three months before the first SN detection and the last ZTF nondetection is on 2018 May 25.17. The SN is visible in data by ATLAS as early as UT 2018 June 15.26, ~ 84 days before the first ZTF detection and 4 days after the previous nondetection. We adopt UT 2018 June 13.25 (JD 2458282.75), the midpoint between the last nondetection and the first detection, as an estimate of the explosion time for this event.

2.4.2. SN 2019ape

SN 2019ape was detected in Pan-STARRS1 data on UT 2019 Feb. 05.39 (JD 2458519.89) at J2000 coordinates of $\alpha = 10^{\text{h}}51^{\text{m}}42^{\text{s}}.5$, $\delta = +18^{\circ}28'52''.73$ at a brightness of $w = 18.57$ mag (Chambers et al. 2019). On UT 2019 February 08.71 (JD 2458523.21) the transient was classified as a SN Ic (Carini et al. 2019) at a redshift of $z = 0.02$ based on the SN features. De et al. (2020) acquired a nebular spectrum of the SN 300 days after explosion and conclude that it does not belong to the Ca-rich group based on the Ca II to [O I] ratio. SN 2019ape was detected in the massive elliptical NGC 3426 ($z = 0.020414$). We adopt the host redshift and a corresponding redshift-dependent distance of 90.4 ± 6.4 Mpc corrected for

Virgo, Shapley, and Great attractor infall. Applying the ZTF forced-photometry pipeline (Masci et al. 2018) yields an earlier detection from UT 2019 January 31.44 (JD 2458514.94), at a brightness of $r = 20.52 \pm 0.19$ mag. The latest nondetection is at >20.9 mag 3 days earlier. We estimate the explosion date as JD 2458513.44 ± 1.5 , the midpoint between the first detection and the last nondetection.

2.4.3. SN 2020uik

SN 2020uik was detected in ATLAS data on UT 2020 Sep. 20.62 (JD 2459113.12) at J2000 coordinates of $\alpha = 08^{\text{h}}01^{\text{m}}54^{\text{s}}.18$, $\delta = -06^{\circ}45'39''.52$ at a brightness of $c = 18.5$ mag (Tonry et al. 2020). On UT 2020 October 18.53 (JD 2459141.03) the transient was classified as a SN II (Dahiwalé & Fremling 2020) at a redshift of $z = 0.03$ based on the SN features. These are consistent with the NED redshift of $z = 0.028156$ of WISEA J080154.84-064527.1, a red galaxy offset by $15''.0$ from the SN location. We adopt the host redshift and a corresponding redshift-dependent distance of 118.1 ± 8.3 Mpc corrected for Virgo, Shapley, and Great attractor infall. SN 2020uik was detected during a plateau in its light curve after a long period in which the field was not observed. Assuming a plateau that extends 100 days since explosion (Arcavi et al. 2017), we estimate an explosion time of around JD 2459085, 28 days prior to the first detection. The best-fitting Superfit template of its first spectrum, taken 56 days after the estimated explosion, is the spectrum of the SN II SN 2013fs (taken 57 days after explosion; Yaron et al. 2017).

2.5. Extinction

We queried the NASA/IPAC NED Galactic Extinction Calculator³⁴ for the foreground Galactic extinction in the line of sight toward each of the 3 SNe presented in this work, derived from the maps of Schlafly & Finkbeiner (2011). We find a line-of-sight extinction of $E_{(B-V,MW)} = 0.043$ mag for SN 2018fsh $E_{(B-V,MW)} = 0.031$ mag for SN 2019ape and $E_{(B-V,MW)} = 0.082$ mag for SN 2020uik. We estimate the host extinction of SN 2019ape (along the line of sight to the SN) using the $g-r$ color curve of SN 2019ape compared to intrinsic color curves of SNe Ic (Stritzinger et al. 2018; Drout et al. 2011). We find $E_{(B-V,Host)} = 0.14 \pm 0.03$ mag. This value

³³ <https://ned.ipac.caltech.edu/>

³⁴ <https://ned.ipac.caltech.edu/forms/calculator.html>

is broadly consistent with the value derived using the equivalent width of the Na D doublet absorption feature (Poznanski et al. 2012). We do not attempt to estimate the host extinction for SN 2018fsh or SN 2020uik, but estimate these are not significant due to the large offset from their host galaxies.

3. Observations

3.1. Photometry

For all SNe discussed in this paper, we acquired *gri* photometry using the P48 ZTF camera (Dekany et al. 2020). These data were processed using the ZTF data-processing system (Masci et al. 2018). Light curves were obtained using the forced-photometry pipeline (Masci et al. 2018) on difference images produced using the optimal image subtraction algorithm of Zackay et al. (2016) at the position of the SN, as reported by the first ZTF alert. We report detections above a 3σ threshold. Same-night detections were binned in order to boost the signal. Additional photometry was acquired with:

1. The Las Cumbres Observatory (LCO) network of 1 m telescopes through the Global Supernova Project (Howell 2019). Photometric data were reduced using the `lcogtsnpipe` pipeline which performs PSF-fitting photometry. Landolt standard field stars were used to calculate the zero-points for the filters *UBV*, whereas for *gri* bands we use Sloan magnitudes of stars in the same field as the object.
2. The two ATLAS 0.5 m telescopes on Haleakala and Mauna Loa, Hawaii, USA (Tonry et al. 2018). Data were reduced using the forced-photometry service (Smith et al. 2020).
3. The 2.0 m robotic Liverpool Telescope (LT; Steele et al. 2004) at the Observatorio del Roque de los Muchachos Observatory on La Palma using the optical imager (IO:O) through the *g*, *r*, *i*, and *z* bands. Photometry was reduced using standard IRAF routines within a custom PYTHON script and stacked using `SWarp` (Bertin et al. 2002). Digital image subtraction was performed versus PS1 reference imaging following the techniques of Fremling et al. (2016) and calibration was performed relative to PS1 photometric standards.
4. The Rainbow Camera (Blagorodnova et al. 2018) on the Palomar 60 inch telescope (P60; Cenko et al. 2006). Reductions were performed using the automatic pipeline described by Fremling et al. (2016).

For SN 2019ape, instrument cross calibration was performed by applying constant shifts calculated using polynomial fits to band-specific light curves. In case a single instrument was available for a given band, the calibration was performed using synthetic photometry on the spectra scaled to *r*-band photometry to ensure accuracy relative to other bands. Following these procedures, a constant shift of -0.32 mag was applied to LCO *g*-band light curves to match the evolution of LT and ZTF light curves. No other offsets were required. The photometry in this work will be made available through the Weizmann Interactive Supernova data REpository (WiSeREP; Yaron & Gal-Yam 2012) upon publication, and is provided in Table 2. The light curves of SN 2018fsh and SN 2020uik are shown in Figure 4, and the light curves of SN 2019ape are shown in Figure 5.

3.2. Spectroscopy

Spectroscopic follow-up of SNe appearing in this work was performed using a variety of instruments:

1. The 3.6 m ESO New Technology Telescope (NTT) at La Silla, Chile, using the ESO Faint Object Spectrograph and Camera (v.2) (EFOOSC2; Buzzoni et al. 1984) as part of ePESSTO+. These data were reduced using the PESSTO pipeline (Smartt et al. 2015).
2. The Nordic Optical telescope (NOT) using The Alhambra Faint Object Spectrograph and Camera (ALFOSC). Reductions were performed using FOSCGUI.³⁵
3. The 200 inch Hale telescope at Palomar observatory using the Double Beam Spectrograph (Oke & Gunn 1982). These data were reduced following standard procedures using the P200/DBSP pipeline described in Bellm & Sesar (2016).
4. The Spectral Energy Distribution machine (SEDm; Blagorodnova et al. 2018) mounted on the Palomar 60 inch telescope. Data were reduced using the automatic SEDm pipeline (Rigault et al. 2019).
5. The Spectrograph for the Rapid Acquisition of Transients (SPRAT; Piascik et al. 2014) on the Liverpool Telescope. SPRAT spectra were reduced using the LT pipeline (Smith et al. 2016) and flux calibrated using a custom PYTHON routine.
6. The Low Resolution Imaging Spectrometer (LRIS; Oke et al. 1995) on the 10-m Keck I telescope. The data were reduced using the LRIS automated reduction pipeline (LPipe; Perley 2019).

Figure 6 shows the spectrum of SN 2018fsh 96 days after explosion in comparison with the best-fitting SN II spectrum at a similar phase using `Superfit`. Figures 7 and 8 show the spectral evolution of SN 2019ape and SN 2020uik, respectively. Table 3 contains a log of spectroscopic observations presented in this work. All spectra will be made available to the public on WiSeREP³⁶ upon publication.

3.3. Host-galaxy Photometry

We retrieved archival images of all SN host galaxies discussed in this work from Galaxy Evolution Explorer (GALEX) Data Release (DR) 8/9 (Martin et al. 2005), SDSS DR9 (Ahn et al. 2012), PS1 DR1 (Chambers et al. 2016), the Two-Micron All Sky Survey (2MASS; Skrutskie et al. 2006), and the unWISE (Lang 2014) images from the NEOWISE (Meisner et al. 2017) Reactivation Year 3. For SNe included in our sample we use the matched-aperture photometry software package `Lambda Adaptive Multi-Band Deblending Algorithm in R` (LAMBDAAR; Wright et al. 2016) that is based on a photometry software package developed by Bourne et al. (2012) and the tools presented by Schulze et al. (2021). The photometry was either calibrated against zero-points (GALEX, PS1, SDSS, and NEOWISE) or against a set of stars (2MASS). We correct the measurements for Milky Way extinction based on Schlafly & Finkbeiner (2011). The resulting photometry is summarized in Tables 4 and 5. We note that in the case of SN 2016hil, the W3 measurements are estimated from the W2 – W3 color reported in

³⁵ <http://graspa.oapd.inaf.it/foscgui.html>

³⁶ <https://www.wiserep.org/>

Table 2
Photometric Observations of SN 2018fsh, SN 2019ape, and SN 2020uik

SN Name	JD	Estimated Time from Explosion (Rest-frame Days)	Instrument	Filter	AB Magnitude
SN 2019ape	2458514.94	1.47	ZTF	<i>r</i>	20.45 ± 0.19
SN 2019ape	2458522.92	9.29	ZTF	<i>g</i>	18.72 ± 0.01
SN 2019ape	2458524.45	10.79	LT	<i>g</i>	18.63 ± 0.01
SN 2019ape	2458524.45	10.79	LT	<i>r</i>	18.07 ± 0.01
SN 2019ape	2458524.45	10.79	LT	<i>z</i>	18.14 ± 0.02
SN 2019ape	2458524.45	10.79	LT	<i>i</i>	18.19 ± 0.01
SN 2019ape	2458526.93	13.22	ZTF	<i>g</i>	18.67 ± 0.03
SN 2019ape	2458528.0	14.27	LT	<i>g</i>	18.63 ± 0.01
SN 2018fsh	2458284.76	4.63	ATLAS	<i>c</i>	17.14 ± 0.03
SN 2018fsh	2458286.76	6.57	ATLAS	<i>o</i>	17.22 ± 0.09
SN 2018fsh	2458371.01	88.44	ZTF	<i>r</i>	18.78 ± 0.02
SN 2018fsh	2458373.99	91.34	ZTF	<i>r</i>	18.78 ± 0.02
SN 2018fsh	2458374.01	91.36	ZTF	<i>g</i>	20.21 ± 0.11
SN 2018fsh	2458376.99	94.26	ZTF	<i>g</i>	20.3 ± 0.05
SN 2018fsh	2458377.02	94.28	ZTF	<i>r</i>	18.86 ± 0.02
SN 2020uik	2459109.11	23.41	ATLAS	<i>o</i>	18.24 ± 0.07
SN 2020uik	2459111.1	25.34	ATLAS	<i>c</i>	18.43 ± 0.04
SN 2020uik	2459113.12	27.3	ATLAS	<i>o</i>	18.27 ± 0.03
SN 2020uik	2459115.09	29.21	ATLAS	<i>c</i>	18.53 ± 0.07
SN 2020uik	2459115.1	29.22	ATLAS	<i>c</i>	18.33 ± 0.12
SN 2020uik	2459126.12	39.92	ATLAS	<i>o</i>	18.11 ± 0.02
SN 2020uik	2459127.12	40.89	ATLAS	<i>o</i>	18.01 ± 0.1
SN 2020uik	2459130.97	44.63	ZTF	<i>r</i>	18.23 ± 0.1

Note. All measurements are reported in the AB system and are corrected for Galactic line of sight reddening. The full table will be made available electronically on the journal website and on WISEREP upon publication.

(This table is available in its entirety in machine-readable form.)

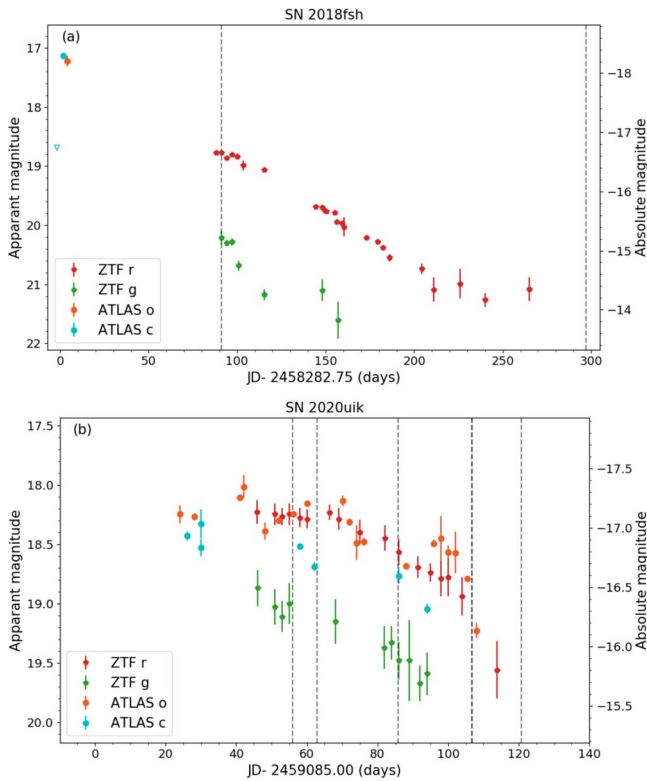


Figure 4. Light curves of SN 2018fsh (a) and SN 2020uik (b). Full symbols are detections and empty triangles are 5σ upper limits. Vertical black dashed lines mark the dates of spectroscopic observations.

Irani et al. (2019), where MIR photometry is measured from ALLWISE data using the same methodology described here.

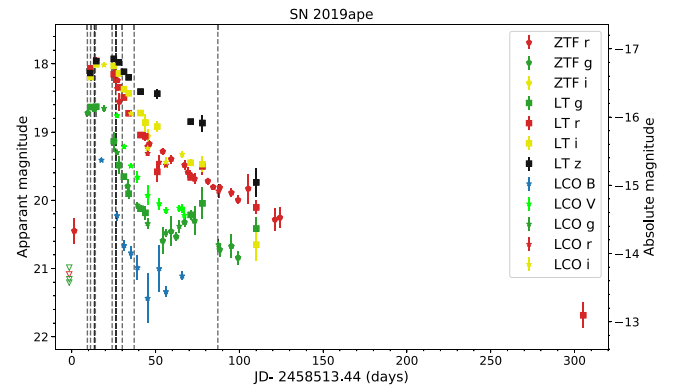


Figure 5. Optical light curves of SN2019ape. Full symbols are detections and empty triangles are P48 5σ upper limits. Vertical black dashed lines mark the dates of spectroscopic observations.

4. Results

In this section we analyze the properties of the three newly discovered SNe. In Section 4.1 we discuss the light curve, spectra, and location of the SNe II SN 2018fsh and SN 2020uik. In Section 4.2 we analyze our observations of SN 2019ape. We argue it is a typical SN Ic by comparing it to other SNe Ic, and by modeling its spectroscopic evolution. We present evidence that the SN has formed near the explosion site and is a result of low-level star formation in its elliptical host. In Section 4.3 we derive host galaxy properties for the combined sample of CCSNe in ellipticals and compare them to the hosts of all BTS SNe (CCSNe and SNe Ia). We discuss these results and their implications for star formation in elliptical galaxies in Section 5.

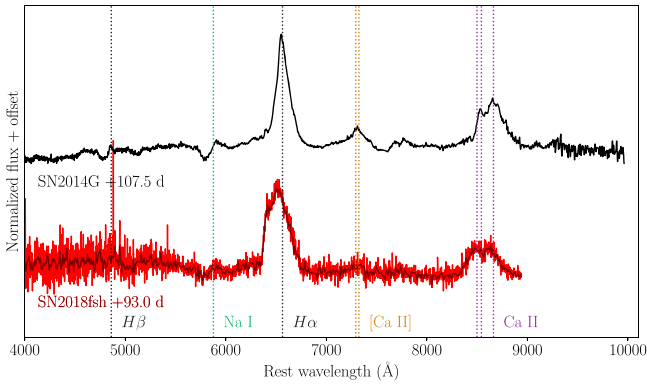


Figure 6. Comparison of the spectrum of SN 2018fsh to the spectrum of the best matching Superfit result SN 2014G at a similar phase. The main elements appearing in both spectra are marked with vertical lines. The dark line is a binned version of the spectrum to guide the eye.

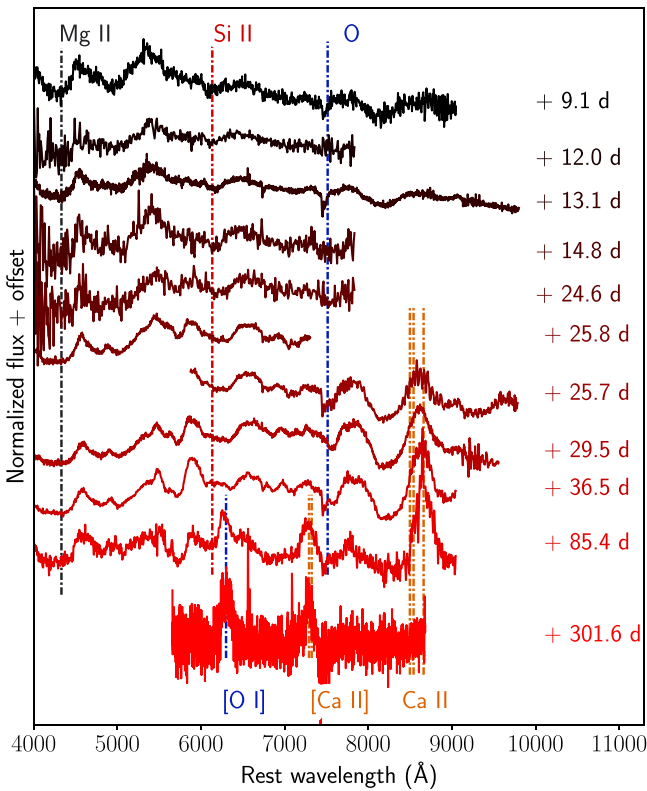


Figure 7. Spectral sequence of SN 2019ape. Phase is denoted in rest-frame days. The main features appearing in the spectrum are marked with vertical lines. Absorption features are blueshifted by $10,000 \text{ km s}^{-1}$.

4.1. SN 2018fsh and SN 2020uik

4.1.1. Light-curve Properties

SN 2020uik is a SN IIP detected early in its plateau phase at an absolute magnitude of $M_r = -16.9$ mag, which we adopt as the peak luminosity. The plateau continues for 65 days until the SN begins to fade. SN 2018fsh is a SN IIL—it was detected by ATLAS near peak at a luminosity of $c = -18.1$ mag and was observed again during its linear decline, 77 days after the estimated time of maximum light. It continues to decline for an additional 150 days until becoming undetectable.

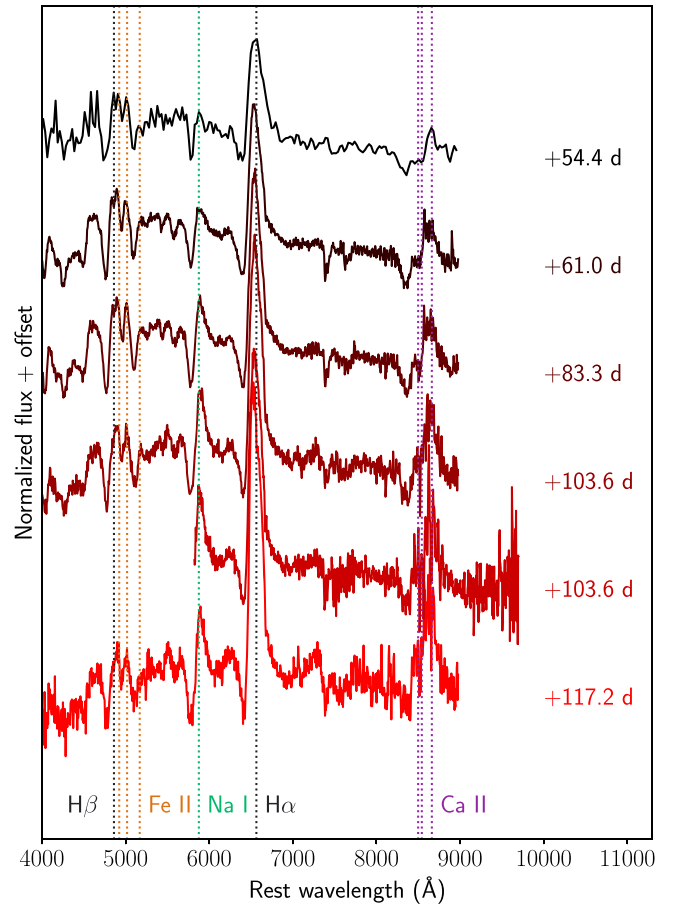


Figure 8. Spectral sequence of SN 2020uik. Phase is in rest-frame days.

4.1.2. Spectra

The spectral observations of SN 2018fsh and SN 2020uik show that both appear to be spectroscopically normal SNe II. SN 2018fsh was observed late in its evolution, and shows a typical spectrum for a SN IIL at this phase. We show a comparison with the closest Superfit match SN 2014G (de Jaeger et al. 2019) in Figure 6. The spectrum shows strong $H\alpha$ and moderate Ca II emission. We interpret the absorption feature at $\lambda 5900$ as Na $\lambda 5890$ and not He $\lambda 5876$ in the absence of additional features at $\lambda 6678$ and $\lambda 7065$ (Gal-Yam 2017). Figure 9 shows a later nebular spectrum with Mg and Ca II emission lines as well as a complex $H\alpha$ emission profile. The $H\alpha$ feature has a broad and boxy profile, with velocities ranging from $-15,000$ to $10,000 \text{ km s}^{-1}$. Similar profiles have been previously attributed to interaction of the fast outer ejecta with CSM (Filippenko et al. 1994; Patat et al. 1995). This interpretation is supported by the flattening of the light curve at late times, e.g., as observed in all bands for SN 1993J (Jerkstrand et al. 2015).

SN 2020uik has a more detailed spectroscopic sequence with a typical $H\alpha$ P-Cygni profile, Na I absorption at $\lambda 5890$ as well as Fe II absorption lines ($\lambda 4924$, $\lambda 5018$ and $\lambda 5169$) and with typical Ca II emission developing over time. Neither of the two events shows significantly strong Ca emission compared to other SNe II to be considered peculiar.

Table 3
Log of Spectroscopic Observations

SN	Date	Estimated Time Since Explosion (rest-frame days)	Instrument	Exposure Time (s)	Airmass	Grism
SN 2019ape	2019 Feb. 08	9.75	NTT/EFOSC2	900	1.49	13
SN 2019ape	2019 Feb. 10	12.56	LT/SPRAT	1200	1.02	red
SN 2019ape	2019 Feb. 12	14.33	P200/DBSP	900	1.05	600/4000
SN 2019ape	2019 Feb. 13	15.39	LT/SPRAT	1200	1.19	red
SN 2019ape	2019 Feb. 23	25.29	LT/SPRAT	1200	1.05	red
SN 2019ape	2019 Feb. 25	26.32	NTT/EFOSC2	2700	1.59	16
SN 2019ape	2019 Feb. 25	26.37	NTT/EFOSC2	2700	1.49	11
SN 2019ape	2019 Mar. 01	30.15	NOT/ALFOSC	2400	1.02	4
SN 2019ape	2019 Mar. 08	37.12	NTT/EFOSC2	2700	1.48	13
SN 2019ape	2019 Apr. 27	86	NTT/EFOSC2	2 × 2700	1.51	13
SN 2019ape	2019 Dec. 03	302.19	Keck/LRIS	1750	1.04	600/4000,400/8500
SN 2020uik	2020 Oct. 18	39.83	P60/SEDM	2250	1.52	IFU
SN 2020uik	2020 Oct. 25	46.44	NTT/EFOSC2	2700	1.13	13
SN 2020uik	2020 Nov. 17	68.69	NTT/EFOSC2	2700	1.35	13
SN 2020uik	2020 Dec. 08	89.03	NTT/EFOSC2	2700	1.35	13
SN 2020uik	2020 Dec. 08	89.06	NTT/EFOSC2	2700	1.19	16
SN 2020uik	2020 Dec. 22	102.6	NTT/EFOSC2	2700	1.27	13
SN 2018fsh	2018 Sep. 12	91.2	P200/DBSP	2 × 600	1.66	316/7500, 600/4000
SN 2018fsh	2019 Apr. 06	291.1	Keck/LRIS	1750	1.655	316/7500, 600/4000

Table 4
Photometry of SN Host Galaxies Analyzed in This Work

Instrument/Filter	λ_{eff} (Å)	SN 2003ky	SN 2006ee	SN 2006gy	PTF10gqf	PS1-12sk
GALEX/FUV	1542	18.92 ± 0.17	17.83 ± 0.03	20.25 ± 0.82	19.83 ± 0.05	19.27 ± 0.14
GALEX/NUV	2274	18.3 ± 0.08	17.85 ± 0.06	18.34 ± 0.24	19.87 ± 0.06	18.24 ± 0.06
SDSS/ <i>u</i>	3595	16.89 ± 0.04	15.12 ± 0.05	15.14 ± 0.14	17.72 ± 0.09	16.54 ± 0.05
SDSS/ <i>g</i>	4640	15.35 ± 0.01	13.43 ± 0.01	13.43 ± 0.08	16.16 ± 0.02	14.82 ± 0.04
SDSS/ <i>r</i>	6122	14.62 ± 0.01	12.63 ± 0.01	12.63 ± 0.04	15.48 ± 0.01	13.99 ± 0.01
SDSS/ <i>i</i>	7440	14.24 ± 0.01	12.19 ± 0.01	12.22 ± 0.04	15.08 ± 0.01	13.56 ± 0.01
SDSS/ <i>z</i>	8897	13.95 ± 0.02	11.83 ± 0.03	11.92 ± 0.03	14.8 ± 0.04	13.27 ± 0.04
PS1/ <i>g</i>	4776	15.38 ± 0.01	13.39 ± 0.03	13.4 ± 0.04	...	14.79 ± 0.06
PS1/ <i>r</i>	6130	14.61 ± 0.01	12.68 ± 0.02	12.67 ± 0.09	15.5 ± 0.01	14.02 ± 0.06
PS1/ <i>i</i>	7485	14.24 ± 0.01	12.28 ± 0.01	12.28 ± 0.04	15.12 ± 0.01	13.64 ± 0.04
PS1/ <i>z</i>	8658	14.07 ± 0.01	12.04 ± 0.02	12.04 ± 0.05	14.95 ± 0.02	13.46 ± 0.04
PS1/ <i>y</i>	9603	13.8 ± 0.03	11.8 ± 0.03	11.83 ± 0.04	14.67 ± 0.05	13.23 ± 0.04
2MASS/J	16620	13.69 ± 0.04	11.56 ± 0.03	11.57 ± 0.02	14.68 ± 0.05	12.87 ± 0.03
2MASS/H	12482	13.37 ± 0.03	11.36 ± 0.03	11.34 ± 0.02	14.43 ± 0.05	12.71 ± 0.04
2MASS/K	21590	13.55 ± 0.04	11.55 ± 0.03	11.51 ± 0.02	14.72 ± 0.05	12.83 ± 0.04
WISE/W1	33526	14.32 ± 0.01	12.34 ± 0.01	12.3 ± 0.01	15.25 ± 0.02	13.6 ± 0.02
WISE/W2	46028	14.96 ± 0.02	13.04 ± 0.01	12.94 ± 0.02	15.85 ± 0.02	14.29 ± 0.02
WISE/W3	120000	14.76 ± 0.06	13.56 ± 0.07	13.03 ± 0.03	15.53 ± 0.07	15.49 ± 0.16
WISE/W4	220000	16.19 ± 0.82	13.82 ± 0.23	12.39 ± 0.04	16.15 ± 0.56	>14.56

Note.

^a All measurements are reported in the AB system and are corrected for Galactic line of sight reddening.

4.1.3. Limits on an Underlying Host Galaxy

We derive limits on the presence of a compact source at the sites of SN 2018fsh and SN 2020uik using deep archival imaging as described in Irani et al. (2019). For SN 2018fsh we use Legacy Survey images (Dey et al. 2019) from the Beijing-Arizona Sky Survey fields (Zou et al. 2017), and for SN 2020uik we use deep PS1 imaging (Flewelling et al. 2020). Our 5σ limits are $m_g > 24.69$ mag at the site of SN 2018fsh and $m_g > 23.45$ mag at the site of SN 2020uik corresponding to luminosity limits of $M_g = -10.73$ mag and $M_g = -11.91$ mag respectively. In Figure 10 we show cutouts

of the explosion sites. In both cases, there are no sources within a few kpc of the SN location.

4.2. SN 2019ape

4.2.1. Light-curve Properties

The light curves of SN 2019ape are shown in Figure 5. SN 2019ape rose to an *r*-band peak luminosity of $M_{\text{peak}} = -16.75 \pm 0.05$ mag, 17.1 ± 0.7 days after the explosion in the SN rest frame. The time of peak is determined by fitting a third-order polynomial to the *r*-band data around the

Table 5
Photometry of SN Host Galaxies Analyzed in This Work (continued)

Instrument/Filter	λ_{eff} (Å)	PTF16pq	SN 2016hii ^b	SN 2018fsh	SN 2019ape	SN 2020uik
GALEX/FUV	1542	19.04 ± 0.11	19.83 ± 0.08	19.47 ± 1.43	17.67 ± 0.05	19.77 ± 0.15
GALEX/NUV	2274	19.36 ± 0.07	20.42 ± 0.17	18.35 ± 0.47	16.57 ± 0.02	18.36 ± 0.06
SDSS/ <i>u</i>	3595	16.25 ± 0.09	17.67 ± 0.08	16.67 ± 0.12	14.89 ± 0.03	...
SDSS/ <i>g</i>	4640	14.49 ± 0.02	15.88 ± 0.03	15.13 ± 0.04	13.36 ± 0.01	...
SDSS/ <i>r</i>	6122	13.66 ± 0.01	15.02 ± 0.02	14.34 ± 0.04	12.59 ± 0.01	...
SDSS/ <i>i</i>	7440	13.22 ± 0.02	14.57 ± 0.02	13.93 ± 0.03	12.2 ± 0.01	...
SDSS/ <i>z</i>	8897	13.0 ± 0.03	14.2 ± 0.04	13.62 ± 0.04	11.91 ± 0.02	...
PS1/ <i>g</i>	4776	14.43 ± 0.02	15.84 ± 0.03	15.08 ± 0.02	13.47 ± 0.01	15.71 ± 0.03
PS1/ <i>r</i>	6130	13.7 ± 0.01	15.09 ± 0.02	13.97 ± 0.02	12.74 ± 0.02	15.09 ± 0.03
PS1/ <i>i</i>	7485	13.31 ± 0.01	14.64 ± 0.01	14.34 ± 0.02	12.46 ± 0.01	14.76 ± 0.03
PS1/ <i>z</i>	8658	13.09 ± 0.01	14.47 ± 0.01	13.79 ± 0.04	12.13 ± 0.01	14.57 ± 0.07
PS1/ <i>y</i>	9603	12.85 ± 0.02	14.16 ± 0.03	13.57 ± 0.07	11.86 ± 0.02	14.3 ± 0.08
2MASS/J	16620	12.59 ± 0.05	14.14 ± 0.05	13.32 ± 0.04	11.63 ± 0.02	14.07 ± 0.04
2MASS/H	12482	12.27 ± 0.05	13.85 ± 0.05	13.18 ± 0.04	11.49 ± 0.03	14.05 ± 0.05
2MASS/K	21590	12.56 ± 0.05	14.03 ± 0.05	13.37 ± 0.05	11.65 ± 0.02	14.28 ± 0.07
WISE/W1	33526	...	14.49 ± 0.01	14.08 ± 0.02	12.36 ± 0.01	15.0 ± 0.02
WISE/W2	46028	14.01 ± 0.02	15.13 ± 0.03	14.78 ± 0.02	13.0 ± 0.01	15.69 ± 0.02
WISE/W3	120000	14.54 ± 0.10	16.2 ± 0.12	16.12 ± 0.45	12.98 ± 0.06	17.16 ± 0.26
WISE/W4	220000	14.69 ± 0.57	14.9 ± 0.12	> 14.83	13.2 ± 0.19	16.35 ± 0.73

Notes.

^a All measurements are reported in the AB system and are corrected for Galactic line of sight reddening.

^b W3 photometry is estimated from the W2-W3 ALLWISE color of Irani et al. (2019) (see text).

peak (10–30 days after t_{exp}), and the error is estimated by varying the fit range and order. The decline of the light curve is observed over the course of 100 days, with a re-brightening of the *g*- and *B*-band light curves observed starting from $t = 60$ days and reaching an unusual secondary peak of $g = -14.6$ mag at $t \sim 80$ days. The transient is then observed again at $t = 305$ days at a luminosity of $r = -13.0 \pm 0.2$ mag before fading below the detection limit. The late-time decline of 2.5 mag over the course of 250 days is consistent with ^{56}Co decay (0.98 mag per 100 days; Woosley et al. 1989), but the exact ^{56}Ni mass cannot be measured directly due to the poor light-curve sampling at late times.

4.2.2. Spectroscopic Comparison of SN 2019ape and Other SNe Ic

Qualitatively, the spectra of SN 2019ape are similar to those of SNe Ic. In Figure 11 the spectra are compared with the well-observed SNe Ic SN 1994I (Filippenko et al. 1995), SN 2004aw, the best-fitting SN to SN 2019ape with Superfit (Taubenberger et al. 2006), and SN 2007gr (Valenti et al. 2008; Modjaz et al. 2014) around maximum light and at two weeks past maximum. Around maximum light, the spectroscopic features are similar in position and in strength among the objects, in particular those associated with Fe II and Mg II in the region bluewards of 5500 Å. Of note is that the spectrum of SN 2019ape at -7.5 days peaked at around 5500 Å. This is unlike the early spectra of SNe 2004aw and 2007gr which are bluer despite being observed later in their evolution (e.g., the spectrum of SN 2007gr at -4.6 days peaks at ~ 4000 Å). Over the course of a week, the spectra of the comparison objects gradually redden as they reach maximum light and the ejecta cool. The SN 2019ape spectrum at -3.5 days is similar in this respect to the comparison objects around peak or slightly after. The spectrum is a very good match to the spectrum of SN 2004aw at around $+5$ days. As time progresses the objects gradually evolve to look similar, although SN 2019ape does not

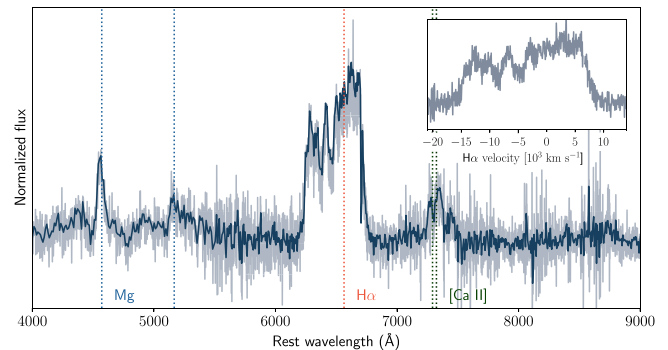


Figure 9. The nebular spectrum of SN 2018fsh. Dashed colored lines denote major features. Inset panel shows a zoom in of the $\text{H}\alpha$ feature with wavelength in units of velocity relative to the rest frame. The dark curve is a binned version of the spectrum to guide the eye.

display the narrow lines of SN 2007gr and retains the slight blending of the Fe II lines in the blue part of the spectrum as seen in SNe 1994I and 2004aw (for a discussion of this, see Prentice & Mazzali 2017). It can be concluded that SN 2019ape is a normal SN Ic supernova, albeit with some differences in its pre-peak spectra, and the peculiar secondary peak in *g*-band.

4.2.3. Photospheric-phase Spectral Modelling

We model the spectra of SN 2019ape with a 1D radiative transfer code which has been used extensively to model the spectra of stripped-envelope SNe (SE-SNe) (e.g., Mazzali et al. 2000, 2002, 2006; Sauer et al. 2006; Prentice et al. 2018b; Ashall et al. 2019; Teffs et al. 2021). The code is described in detail by Mazzali & Lucy (1993), Lucy (1999), Mazzali (2000), and is the source of a parameter study by Ashall & Mazzali (2020). The model requires an input density profile, ejecta composition, photospheric velocity, epoch, and luminosity which it then uses to approximate the expanding SN ejecta,

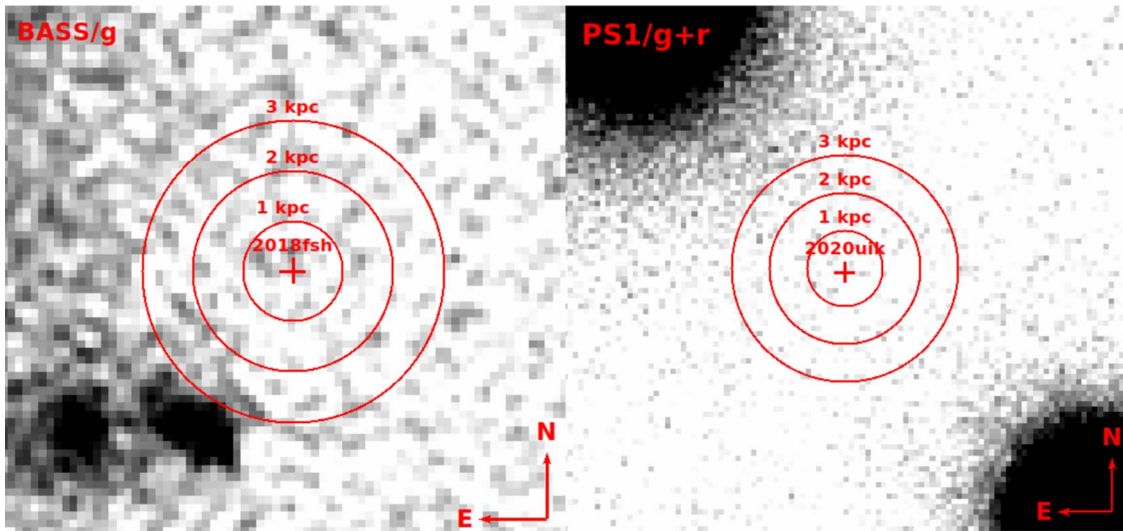


Figure 10. Deep archival images of the explosion sites of SN 2018fsh and SN 2020uik. PS1 g and r images were stacked to increase the signal at the site of SN 2020uik. Concentric circles at 1, 2, 3 kpc are shown around the SN position.

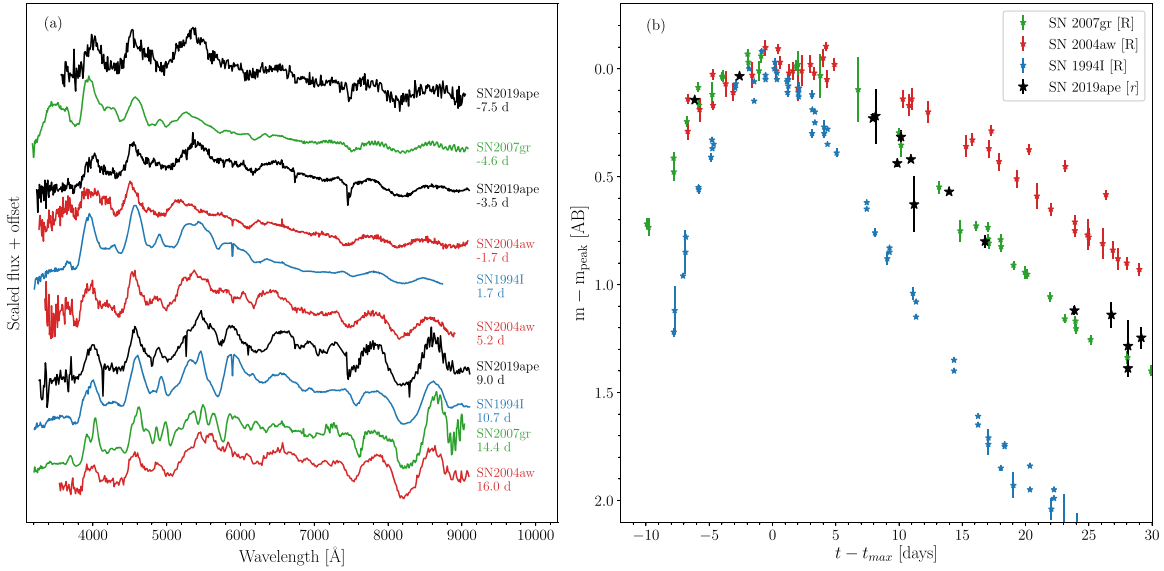


Figure 11. Comparison of the (a) spectra and (b) r/R -band light curves of SN 2019ape to those of SN 2007gr (green), SN 2004aw (red), and SN 1994I (blue). The spectra are corrected for both host and Milky Way extinction as described in the text.

which are assumed to be in homologous expansion. Radiation is assumed to be emitted at a sharp inner boundary (the “inner photosphere”), following a blackbody distribution with temperature T_{bb} , which is found through an iterative MC process. The code follows the propagation of “photon packets” through the SN atmosphere, as represented by the density and abundance profiles. These packets can be subject to Thomson scattering and line absorption in the model ejecta, both fluorescence and reverse fluorescence are possible. The interaction of photons and the gas redistributes the temperature and determines the ionization and excitation states of the gas, which are computed self-consistently using the nebular approximation (Abbott & Lucy 1985; Pauldrach et al. 1996). Finally, the emergent spectrum is found by calculating the formal integral of the radiation field.

We modeled three spectra of SN 2019ape, one prior to r -band maximum, one at maximum, and one a few weeks later. As SN 2019ape shows spectral similarities to SN 2004aw, we

started with the density profile and abundance distribution from the model found in Mazzali et al. (2017), which in turn is based on the CO21 1D hydrodynamical model developed for SN 1994I (Nomoto et al. 1994). This initial model was modified using the scaling relations from Hachinger et al. (2009) for the ejected mass M_{ej} and the explosion kinetic energy E_k until a model that reasonably reproduces the spectral flux and line profiles is found, and then the abundances are iteratively modified until the bulk of the features are well reproduced. As we did not model the light curve in parallel with the spectra, the values of M_{ej} and E_k that we determined are approximate. Additionally, the lack of early-time spectra and photometry limit the accuracy of the determination of E_k using this method (see Mazzali et al. 2017). Our modeling suggests that a good fit is obtained using a density profile with $M_{\text{ej}} = 2 M_{\odot}$ and $E_k = 2 \times 10^{51}$ erg, and a specific kinetic energy that is similar to SN 2004aw ($E_{k,51}/M_{\text{ej}} \approx 1$). As the first modeled epoch is approximately 10 days after t_{exp} as

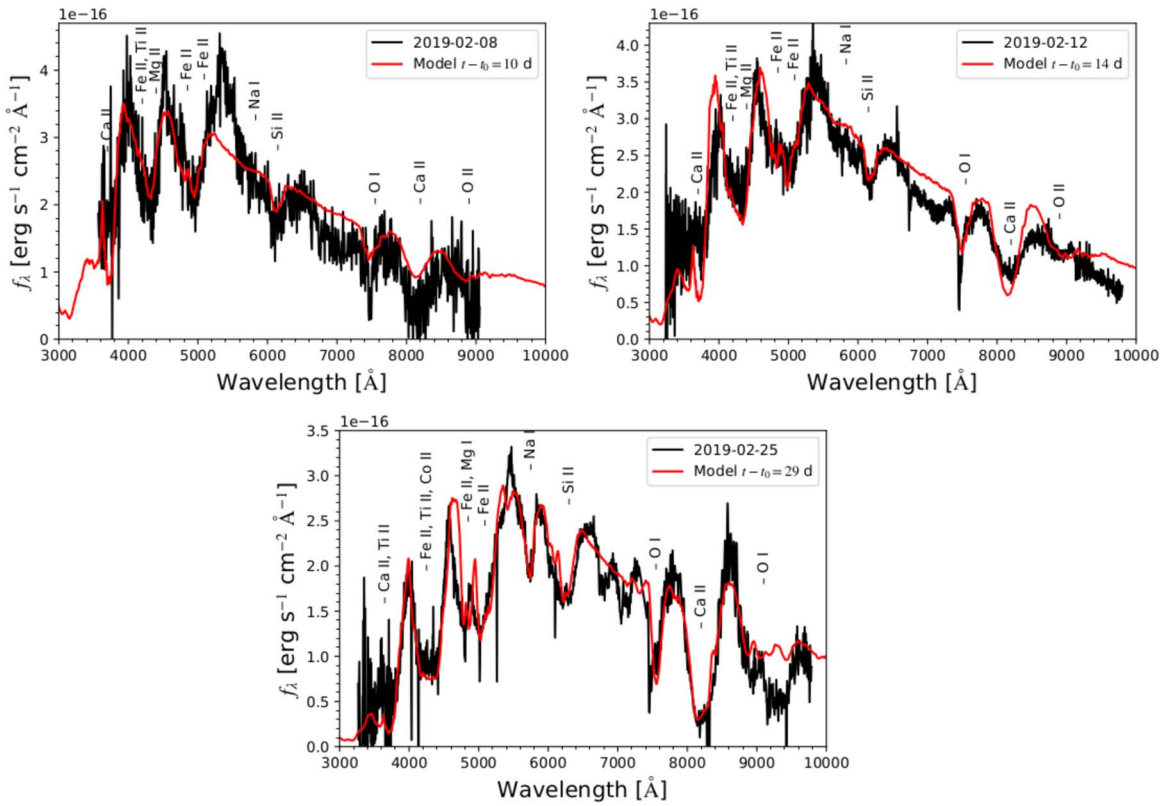


Figure 12. Best-fit model spectra for the selected spectra of SN 2019ape.

Table 6
Parameters and Selected Abundance Fractions for the Model Shells

t (days)	v_{ph} (km s $^{-1}$)	T_{bb} (K)	C	O	Ne	Na	Mg	Si	S	Ca	^{56}Fe	^{56}Ni
Dummy shell	23000	...	0.7	0.004	0.29	0.0	0.005	0.0005	0.00025	0.0	0.0001	0.0001
Dummy shell	17000	...	0.7	0.0065	0.29	0.0	0.0025	0.0005	0.00025	3×10^{-6}	0.0001	0.0001
10	12500	7249.6	0.66	0.035	0.3	0.0005	0.0025	0.0015	0.0006	7×10^{-6}	0.0001	0.0005
14	10500	7028.2	0.5	0.2	0.3	0.00055	0.001	0.0022	0.002	0.0	0.0005	0.002
Dummy shell	8500	...	0.5	0.3	0.15	0.001	0.001	0.015	0.035	2×10^{-6}	0.0025	0.0025
27	6500	6327	0.5	0.3	0.02	0.002	0.001	0.015	0.05	1×10^{-6}	0.0025	0.05

estimated in Section 2.4.2, we used two dummy shells to model the high-velocity material properly. As we have no early spectra, these two shells were primarily used to reduce high-velocity line formation of certain elements. In addition, we use an additional dummy shell between the second and third modeled epochs ($t \sim 14$ days and $t \sim 27$ days respectively) as this is an extensive gap in spectral evolution. The resulting models are shown in Figure 12 with the abundances of each shell given in Table 6.

The first modeled spectrum was obtained on 2019 February 8, ~ 10 days from estimated explosion time and ~ 7.6 days prior to r -band peak. For this spectrum we find $v_{\text{ph}} = 12,500$ km s $^{-1}$ and $L = 1.40 \times 10^{42}$ erg s $^{-1}$. The model manages to capture many of the spectral features well, with a few issues (see first panel of Figure 12). The abundance at this phase is primarily carbon ($\sim 66\%$), with $\sim 30\%$ neon and only 3% oxygen. A larger oxygen abundance leads to an excessively strong O I $\lambda 7774$ feature in the synthetic spectrum. In the dummy shells above this photosphere, the oxygen mass is reduced even further, leaving a C and Ne rich outer shell. Comparatively, at

this epoch the models shown in Mazzali et al. (2017) had approximately equal abundances of carbon and oxygen (35%). The observed O I $\lambda 7774$ line in this epoch is also noisy and likely contaminated with a telluric line, which makes it difficult to fit. As mentioned previously, a key difference between SN 2004aw and SN 2019ape is that the spectrum of SN 2019ape is redder and peaks at ~ 5500 \AA rather than ~ 4500 \AA . Two noticeable issues with the model are the inability to replicate the peak near 5500 \AA and the weak NIR Ca II line. The peak could be driven by re-emission from the iron features near 5000 \AA or possibly other Fe-group elements, however, the high abundances of Fe or Fe-group elements needed to drive the flux upward in this region produce absorption features that are far too strong as well as other lines that are not observed. Increasing the total luminosity can also reproduce the peak at 5500 \AA but produces far too high a flux level at wavelengths redder than 6000 \AA . The second issue is that the Ca II NIR feature is too weak, which is likely due to the model having too high a temperature at this phase, leading to the over-ionization of Ca. Lowering the temperature produces a

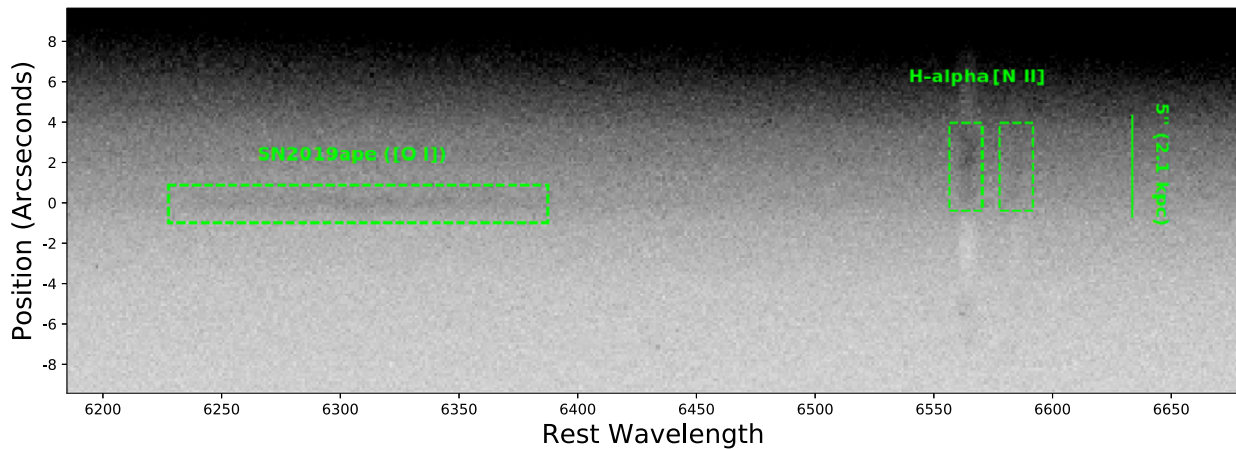


Figure 13. 2D cutout of the nebular spectrum of SN 2019ape. The trace of the SN is faint and becomes significant relative to the galaxy background only at the [O I] nebular feature. Both the H α and weaker [N II] narrow lines extend to the SN site, indicating an underlying star-forming region. The 2D frames are sky subtracted using the sky-subtraction routine of `LPipe`, which removes some of the host-galaxy emission lines for larger galaxies.

worse fit to other parts of the spectrum, and increasing the Ca abundance is inconsistent with the later spectra.

We next model a spectrum that was obtained four days later, on 2019 Feb. 12 (~ 14 days after the explosion and 2.8 days before the peak). The input parameters were $v_{\text{ph}} = 11000 \text{ km s}^{-1}$ and $L = 1.64 \times 10^{42} \text{ erg s}^{-1}$. This spectrum is quite similar to the one at $t - t_{\text{exp}} \sim 10 \text{ d}$ but is marginally redder, suggesting a lower temperature. The abundances are similar to those of the previous spectrum, as the velocities only differ by 1500 km s^{-1} and therefore represent shells located close within the ejecta profile. Although the main features of the spectrum are replicated, owing to the lower temperature the Ca II NIR and H&K features are stronger in this model than in the previous one.

The final spectrum modeled was obtained on 2019 Feb. 25, ~ 27 days after the explosion and 9.4 days after the peak. Here, we used $v_{\text{ph}} = 6500 \text{ km s}^{-1}$ and $L = 1.23 \times 10^{42} \text{ erg s}^{-1}$. As before, many of the features in the spectrum are replicated by the model, apart from the peak at 5500 \AA , which shows an Fe II line with a rest wavelength of 5534 \AA that is clearly not visible in the observed spectrum. Comparing to the other SNe of similar epochs in Figure 11, the line is seen in SN 2004aw, SN 2007gr, and possibly in SN 1994I. However, the Fe abundance is required to reproduce other features, suggesting that the Fe abundance at higher velocities may be too low. But, as discussed previously, increasing the Fe abundance in the outermost regions produces unwanted lines in those epochs. Several lines are observed in the spectrum in the region between 6600 and 7100 \AA that are not reproduced by the model. These are often blends of C I and Fe-group elements. Carbon is still mostly singly ionized, and the issues with the Fe distribution still holds. The O I abundance is still low during this phase, but the O I 7774 \AA line is saturated, and is less responsive to abundances changes at this epoch. The absorption near 9300 \AA is possibly due to strong C I features that are only partially replicated.

4.2.4. Star Formation of the Host Galaxy

Massive stars are associated with regions of elevated star formation which can be traced by UV continuum and H α emission (Kennicutt 1998). Here we consider both star formation in the local environment of SN 2019ape and the total star formation rate of its host galaxy. De et al. (2020)

acquired a deep nebular spectrum of SN 2019ape ~ 300 days after the explosion. The 2D spectrum reveals a compact H α -emitting region in close proximity to the SN site on top of the narrow absorption feature observed throughout the slit. In Figure 13, we show a cutout of the 2D image with the trace of SN 2019ape and the H α emitting region highlighted. Using `SAOImageDS9` (Joye & Mandel 2003) we measured the strength of the H α emission relative to the local absorption background. After correcting for MW extinction we find a flux of $f_{\text{H}\alpha} = 1.4 \pm 0.5 \times 10^{-16} \text{ erg s}^{-1} \text{ cm}^{-2}$ and an integrated H α luminosity of $3.1 \pm 1 \times 10^{38} \text{ erg s}^{-1}$ - a typical value for an H II region (Kennicutt & Edgar 1989). We convert this to a star formation rate (SFR) using the calibration by Kennicutt (1998) and find that this regions forms $2.4 \times 10^{-3} M_{\odot} \text{ yr}^{-1}$. Globally the host galaxy is relatively UV bright, with a color of $\text{NUV} - r_{\text{PS1}} = 4.03 \pm 0.03 \text{ mag}$ indicating it has undergone an episode of recent ($< 100 \text{ Myr}$) star formation. (Suh et al. 2011; Yi et al. 2005).

4.3. Host-galaxy Sample Properties

We use the host photometry of the objects in our sample and the archival photometry for the BTS SN hosts to derive their SFR and stellar masses. Traditionally, SFR can be derived using UV luminosities that are dominated by massive stars (e.g., Kennicutt 1998; Salim et al. 2007). However, this tracer is sensitive to dust attenuation (e.g., see Calzetti et al. 1995; Buat et al. 1999). To compensate for the effects of dust attenuation, we use the UV SFR indicator calibrated by Salim et al. (2007). Stellar mass values are estimated from the W2 brightness using the calibration of Wen et al. (2013). We report the derived SFR and stellar mass estimates in Table 7, along with the mean SFR and stellar mass estimates for Galaxy Zoo spirals and ellipticals. In Figure 14 we plot the SFR of BTS CCSNe hosts, our sample of CCSNe in elliptical galaxies and BTS SNe Ia in elliptical galaxies. The elliptical host galaxies of CCSNe show more star formation on average compared to the general elliptical galaxy population - $0.41^{+0.53}_{-0.23} M_{\odot} \text{ yr}^{-1}$ compared to $0.09^{+0.09}_{-0.05} M_{\odot} \text{ yr}^{-1}$ for Galaxy Zoo ellipticals and $0.76^{+1.47}_{-0.72} M_{\odot} \text{ yr}^{-1}$ for the general CCSN host-galaxy population. CCSNe in elliptical galaxies are also more massive than most elliptical galaxies, with $2.76^{+3.24}_{-1.49} \times 10^{10} M_{\odot}$ compared to an average of $0.83^{+1.95}_{-0.58} \times 10^{10} M_{\odot}$ for the Galaxy Zoo

Table 7
SN Host-galaxy Properties Derived in This Work

SN	Host	SFR ($M_{\odot} \text{ yr}^{-1}$)	Mass ($10^9 M_{\odot}$)
SN2003ky	NGC 4001	1.18 ± 0.09	37.5 ± 1.0
SN2006ee	NGC 774	0.17 ± 0.01	19.6 ± 0.5
SN2006gy	NGC 1260	0.18 ± 0.04	36.4 ± 1.0
PTF10gqf	WISEA J150350.31 +553738.	0.26 ± 0.01	13.9 ± 0.4
PS1-12sk	RXC J0844.9+4258	1.62 ± 0.09	98.7 ± 3.0
SN2016hil	WISEA J011024.51 +141238.	0.26 ± 0.05	50.9 ± 1.9
PTF16pq	CGCG 091-056	0.16 ± 0.01	32.7 ± 0.9
SN2018fsh	MCG +07-18-013	0.43 ± 0.19	15.2 ± 0.4
SN2019ape	NGC 3426	1.22 ± 0.02	49.0 ± 1.3
SN2020uik	WISEA J080154.84- 064527.	0.4 ± 0.02	5.6 ± 0.2
...	Galaxy Zoo ellipticals ^a	$0.09^{+0.09}_{-0.05}$	$8.27^{+19.33}_{-5.79}$
...	Galaxy Zoo spirals ^a	$0.43^{+0.78}_{-0.28}$	$2.43^{+5.69}_{-1.71}$

Note.

^a Values quoted here represent the sample mean and standard deviation.

ellipticals. The high SFR of CCSNe elliptical hosts can be explained by their higher mass. The specific SFR (sSFR; i.e., the SFR per unit mass) of CCSNe elliptical hosts is $1.49^{+2.08}_{-0.87} \times 10^{-11} \text{ yr}^{-1}$ compared to $1.06^{+1.03}_{-0.52} \times 10^{-11} \text{ yr}^{-1}$ for galaxy zoo ellipticals, and $2.60^{+4.99}_{-2.54} \times 10^{-10} \text{ yr}^{-1}$ for the hosts of BTS CCSNe.

5. Discussion

In this paper, we have presented and analyzed three CCSNe occurring in elliptical galaxies from the ZTF BTS experiment and their hosts. In this section we will discuss the implications of our results regarding star formations in ellipticals, as inferred from the population of CCSNe which they host.

5.1. CCSNe as Representative Members of Their Spectroscopic Classes

Finding a CCSN in an elliptical galaxy can be either a sign of residual star formation, or that the progenitor of the event in question was not a massive star. The most recent example of the later are the class of Ca-rich Type Ib supernovae (Perets et al. 2010). While these transients have spectra consistent with SNe Ib near maximum light, they occur predominantly in passive environments and galaxy outskirts, which argues against a massive star origin (e.g., Perets et al. 2010; Kasliwal et al. 2012; Lunnan et al. 2017, and most recently De et al. 2020). In addition to their remarkable locations, Ca-rich SNe display peculiar features—strong Ca emission lines in their nebular phase, and a lower luminosity compared to typical SNe Ib.

A non-massive-star origin has been suggested for individual CCSNe offset from elliptical galaxies, such as (1) for PS1-12sk (Sanders et al. 2013; Hosseinzadeh et al. 2019), where deep HST UV imaging excludes local star formation, and (2) for SN 2016hil (Irani et al. 2019), where a double peaked light curve and a low metallicity spectrum were observed. However, conclusions regarding the (potentially) peculiar properties of CCSNe in elliptical host galaxies were difficult to reach based on isolated events, and due to noisy and sparsely sampled photometry and spectroscopy in the case of SN 2016hil.

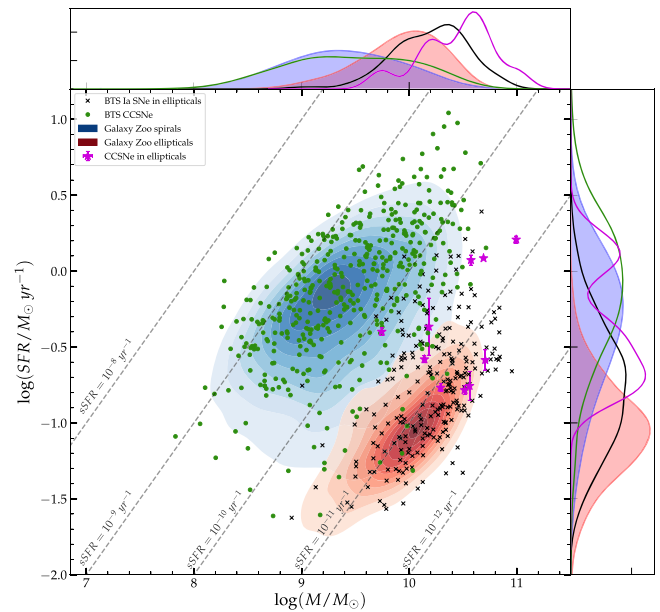


Figure 14. SFR and stellar masses for (1) BTS SNe Ia in elliptical galaxies (black crosses), (2) BTS CCSNe (green circles), (3) our sample of CCSNe in ellipticals (magenta stars). Diagonal gray dashed lines are lines of equal sSFR, and red and blue contours correspond to Galaxy Zoo ellipticals (which satisfy the color criteria described in Section 2) and Galaxy Zoo spirals. The top and right panels show the corresponding 1D kernel density estimates using the same color scheme as the 2D plot.

Here, we consider the combined properties of SNe II in ellipticals, which we can now study as a population. Figure 15 shows the peak luminosities of Type II SNe analyzed in this work, compared to the peak-luminosity distribution of BTS SNe II in our comparison sample. With only 7 SNe II, our sample is too small for a meaningful two-sample Kolmogorov–Smirnov (KS) test of the two peak luminosity distributions. We compare the mean and the standard deviations of the two distributions instead. Our sample of SNe II in ellipticals has a mean peak absolute magnitude of -17.3 ± 1.0 mag, consistent with -17.8 ± 0.8 mag for all spectroscopically regular SNe II in the BTS sample.

Unfortunately, we do not have enough data to compare the spectral properties of SNe II in ellipticals to the general SN II population. However, we point out that absence of strong Ca emission in the nebular spectrum of SN 2018fsh and SN 2019ape, (compared to Ca-rich SNe Ib/c or Ia; De et al. 2020), and the typical spectral evolution of SN 2020uik, suggest these two SNe are typical SNe II. The complex $H\alpha$ profile seen in the nebular spectrum of SN 2018fsh has a broad and boxy profile, extending to high-velocities. These were previously seen for the well observed SN 1993J and SN 1998S and interpreted as signatures of late-time interaction with circumstellar material (Filippenko et al. 1994; Patat et al. 1995; Pozzo et al. 2004). Sollerman et al. (2021) discuss SNe with similar nebular $H\alpha$ extensively. The presence of extended circumstellar material (CSM) around the progenitor of SN 2018fsh could indicate some SNe II form through exotic formation channels, such as mergers of intermediate-mass stars as outlined in Zapartas et al. (2017), or a common-envelope phase as suggested by Soker (2019). Zapartas et al. (2017) estimates that such binary interaction could account for up to 15% of SNe II. It remains to be seen if such signatures are common for SNe II with elliptical host galaxies.

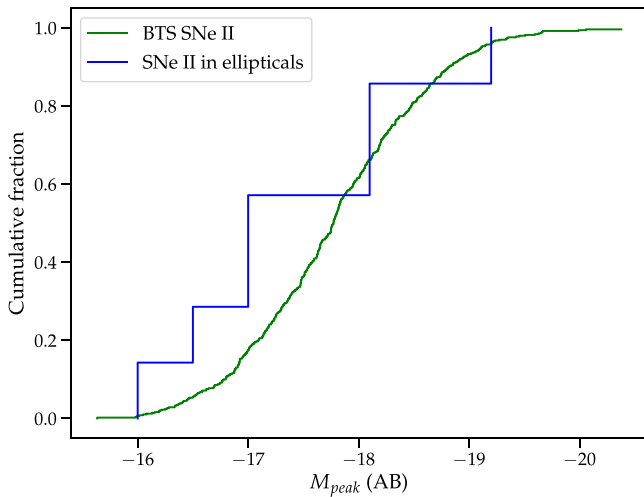


Figure 15. The peak r -band absolute magnitude cumulative distributions for SNe II in elliptical galaxies (blue curve) compared to SNe II from the BTS survey (green curve).

While our sample only contains a single SN Ic, we demonstrated in Section 4.2.2 that SN 2019ape is not a unique event in most respects—both by comparison to other events and by our modeling of SN 2019ape in 4.2.3. The later indicates that the abundances, ejected mass and kinetic energy are typical of a normal SN Ic when compared to a sample of events (Prentice et al. 2016, 2018a). Its peak luminosity of $M_r = -16.75$ mag is close to the mean peak luminosity in the BTS sample (-17.3 ± 0.5 mag) and the light-curve evolution is typical (Prentice et al. 2018a). The only unusual aspect is the secondary g -band peak. It might indicate interaction with extended CSM at later times, as for example observed by Ben-Ami et al. (2014) or Gutiérrez et al. (2021). Similarly to SN 2018fsh, the presence of extended CSM might indicate binary evolution is responsible for the formation of the progenitor star of SN 2019ape. However, given the rest of its properties and the location of the event, we consider it unlikely that SN 2019ape emerged from an unusual SN Ic progenitor. In particular, the estimated ejected mass, chemical abundance (dominated by unburned carbon) and energy point toward a massive progenitor. We conclude that our sample of events in elliptical galaxies is overall consistent with having properties similar to the general population of CCSNe.

5.2. Localized Star Formation in Elliptical Galaxies

Based on our observations of the SN sites, we can separate the sample of CCSNe in ellipticals into two groups—the SNe which are located close to compact star-forming knots, and those that are not. A good example of the former is SN 2006gy, which exploded near the center of an early-type galaxy (Ofek et al. 2007; Smith et al. 2007). SN 2006gy exploded near a region showing signs of localized star formation. This is indicated by a nearby dust lane and compact $H\alpha$ emission interpreted as an H II region (Ofek et al. 2007; Smith et al. 2007). However Jerkstrand et al. (2020) identify neutral iron lines in one of the spectra of SN 2006gy, and argue it is consistent with a SN Ia embedded in a shell of circumstellar material, possibly contradicting a massive star origin. Similarly to the site of SN 2006gy, the localized $H\alpha$ emission extending to the site of SN 2019ape is most likely an indication of a nearby H II region where the progenitor star could have been

formed. SNe Ic are often associated with $H\alpha$ emission in their host galaxies, supporting a young progenitor population even when compared to other CCSNe types (Anderson et al. 2015). The same might be true for SNe Ic observed in elliptical galaxies. This would imply that the initial mass function of stars formed in H II regions in elliptical galaxies extends to massive ($\geq 8 M_\odot$) stars.

5.3. Extended Star Formation or Faint and Diffuse Satellites?

In addition to SNe occurring near sites of active formation, we identify a second group of SNe that occurs in the outskirts of their elliptical hosts, with no signs of localized star formation. In all cases in which the background from the apparent host galaxy was faint enough, we obtain strong limits on the presence of an underlying host galaxy. Limits on the luminosity of hypothetical faint hosts range from -10 mag to -12 mag, putting all these hosts at the low end of the CCSN host-galaxy luminosity distribution as presented in Schulze et al. (2021).

Next, we consider whether CCSNe are typically located at larger offsets from their elliptical host galaxies compared to the host-offset distribution of the general CCSN population, and compared to offsets of SNe Ia in elliptical galaxies. We begin by inspecting the comparison between the offset distributions of SNe Ia in ellipticals and our sample of CCSNe in ellipticals. The right panel of Figure 16 shows the offset distribution of the BTS SNe Ia in ellipticals, CCSNe, and the combined sample of CCSNe in ellipticals. We show only SNe that are offset by less than 30 kpc (projected) or $90''$, the limits of the automatic cross checks presented by Perley et al. (2020). We expect this to cover the vast majority of CCSNe, as the largest offsets in the (i)PTF sample were 37 kpc (Schulze et al. 2021). On the left panel of the same figure we show the physical offsets and the corresponding host-galaxy mass, along with the average 80% light radius, $r_{80}[M_*]$, derived using the low-redshift mass-size relation of Mowla et al. (2019). Schulze et al. (2021) demonstrated (their Figure 11) that the majority ($>85\%$) of CCSNe occur at distances smaller than r_{80} .

The number of SNe in our sample is too low for significant results from a two-sample KS test, but we can formulate an alternative statistical test. We observe that 5% of SNe Ia with elliptical host galaxies are detected at projected offsets larger than 22.5 kpc. We define the null hypothesis as the case in which CCSNe in ellipticals come from the same offset distribution as SNe Ia: For a total of 9 SNe, we expect on average ~ 0.5 SNe at offsets larger than 22.5 kpc (upper 5% of the Ia sample distribution). Assuming a Poisson distribution, the probability of finding three or more SNe in this range is then 1%, so that the null hypothesis is rejected with a confidence of 99%. We note that this test is sensitive to the position of the threshold. For example, repeating this test for all SNe at distances larger than 17 kpc (upper 10% of the Ia sample distribution) will result in less significant results (95% rejection). Repeating this analysis with $r/r_{80}[M_*]$ gives similar results—the probability that 3 of 9 SNe have offsets larger than $>2 r_{80}$ is less than 3%, assuming the offset distribution of SNe Ia with elliptical hosts. To conclude, we find tentative evidence that CCSNe are typically located at larger offsets from their host galaxies compared to SNe Ia in the same host-galaxy population. However, a larger sample is needed in order to reach a high statistical significance.

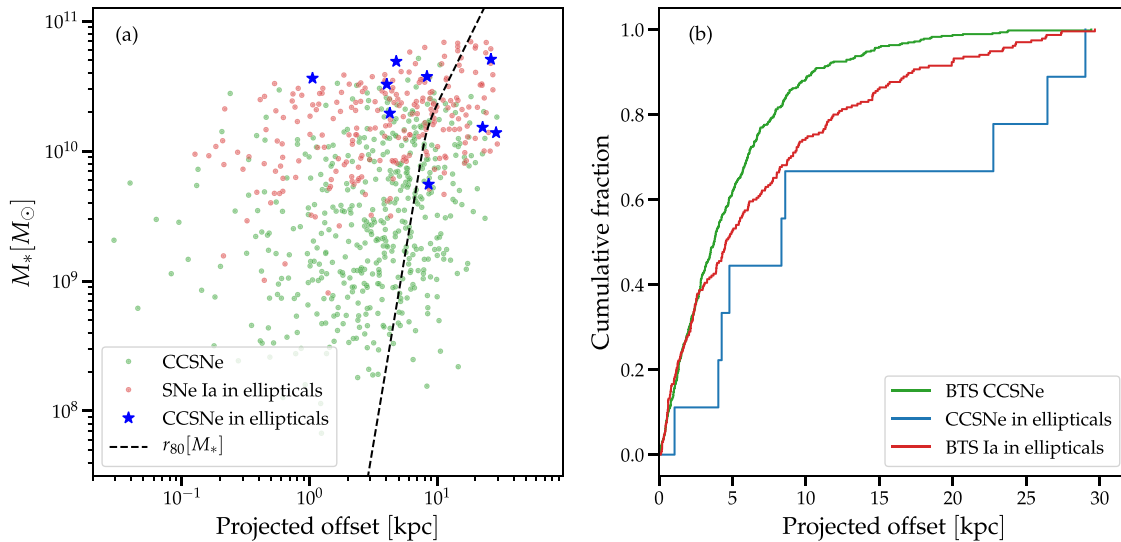


Figure 16. Panel (a) shows the projected physical offsets of CCSNe in ellipticals (blue stars) and stellar mass of their host galaxies. BTS Ia in ellipticals (red circles), and BTS CCSNe (green circles) are shown for comparison. The black dashed line represents the average 80% light radius corresponding to the host-galaxy stellar mass. Panel (b) shows the cumulative distribution of the physical offsets for all three SN populations using the same color scheme.

A possible explanation for the high offset of CCSNe in elliptical galaxies is a reduced detection efficiency at low offsets on top of the high surface brightness center of their elliptical hosts. Foley (2015) suggested this option to explain the lack of Ca-rich SNe Ib at low offsets from their host galaxies. Frohmaier et al. (2017) calculated the recovery efficiency of the PTF pipeline and found it was lower in regions of high surface brightness, but Frohmaier et al. (2017) later found that this is not enough to explain the large offsets observed for Ca-rich transients (Kasliwal et al. 2012). ZTF data should be less susceptible to this bias than PTF was, since the new ZTF camera provides substantially higher image quality, and the optimal image subtraction of Zackay et al. (2016) provides much cleaner subtraction; we thus estimate this effect should be even weaker in our BTS sample. Still, a larger homogeneous sample is needed to quantify this effect for CCSNe in elliptical host galaxies.

An extended offset distribution for CCSNe in elliptical host galaxies compared to the progenitors of SNe Ia has significant implications for the formation of their progenitor stars.

An offset between the locations of SNe Ia and CCSNe in ellipticals could reflect an inside-out growth (Sánchez-Blázquez et al. 2007; Pérez et al. 2013) in some massive ellipticals. While the SNe Ia originate from an older stellar population closer to the center of the massive hosts, CCSNe could explode in regions where the host galaxy is accreting gas from the IGM. This would be in agreement with the findings of Salim et al. (2012), who found galaxy-scale star formation in UV-excess early-type galaxies can extend to large offsets. Gomes et al. (2016) found the extended star formation in the periphery of early-type galaxies can take the form of faint ($24 \lesssim \mu_r(\text{mag}/\square'') \lesssim 26$) spiral features which possibly indicate inside-out growth. However, such low-surface-brightness features are excluded for both SN 2016hil and PS1-12sk, but are still an option for SN 2018fsh SN 2020uik and PTF10gqf.

It is possible that the SNe we observe do not originate from the ellipticals themselves, but from a different stellar population nearby. This option is supported by some evidence that the space between elliptical galaxies might not be completely empty. In addition to having a large offset distribution

extending to regions with apparently no stellar populations (Kasliwal et al. 2012), Ca-rich SNe prefer group and cluster environments (Lunnan et al. 2017). Interestingly enough, PS1-12sk exploded in a bright cluster environment as noted by Sanders et al. (2013), who raised the possibility this might be evidence for star formation in galaxy cluster cooling flow filaments. Similarly, SN 2018fsh occurred in the compact group V1CG 538 (Lee et al. 2017).

However, out of five objects that do not coincide with their elliptical host galaxy, only two are possibly associated with a group or cluster environment. We consider this preliminary evidence that star-forming cooling flows are not the main channel of star formation near elliptical galaxies. Gal-Yam et al. (2003) measured the fraction of cluster SNe Ia originating from an intergalactic stellar population (i.e., those which originate outside of galaxies) to be 20%. In our sample, all SNe detected in group or cluster environment were offset from their putative host, indicating that this fraction is significantly different in CCSNe near ellipticals. However, a larger sample is needed to measure this fraction with high significance. While not part of our sample, we also note that the SN II A399 11 19 0 (Graham et al. 2012) occurred in a nearby galaxy cluster, and is not offset from its host galaxy. Ruiz et al. (2014) explore a sample of 1000 ellipticals and find that the majority have small satellites (down to a mass ratio of 1:400) with an average projected distance of ~ 59 kpc from their parent galaxy, that contain 8% of their stellar mass. However, such galaxies are excluded by our deep limits at the SN sites. Another possibility for the origins of offset CCSNe can be found in the work of Sedgwick et al. (2019), who recently demonstrated that a population of star-forming low-surface-brightness galaxies (LSBGs) host many of the seemingly hostless SNe. These LSBGs can have significant star formation activity, like the nearby UGC 2162. This ultra-diffuse galaxy has a low (but not negligible) SFR of $0.01 M_{\odot} \text{ yr}^{-1}$, but with a very low surface brightness of $24.4 \text{ mag}/\square''$ (Trujillo et al. 2017). This would translate to an integrated absolute magnitude of -7 mag in the optical. Such a faint and extended object would be difficult to detect when located on top of the diffuse emission at the outskirts of a massive elliptical at a redshift of 0.02. While such

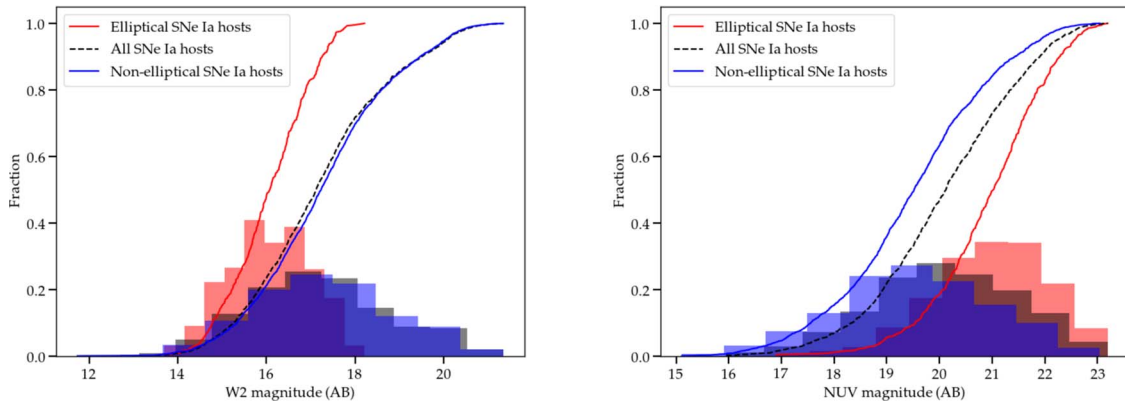


Figure 17. W2 (left) and NUV (right panel) magnitude distribution for all BTS SNe Ia, BTS SNe Ia in elliptical galaxies and BTS SNe Ia in nonelliptical galaxies.

an ultra-diffuse host is ruled out in the case of PS1-12sk (Hosseinzadeh et al. 2019), it has not been excluded for SNe II in the outskirts of elliptical galaxies.

If the host galaxies of offset CCSNe are satellites of massive galaxies, they would constitute a small fraction of CCSNe in their typical host galaxies, and could erroneously be associated with nearby more luminous hosts. However, in elliptical galaxies which host much fewer CCSNe, such satellite galaxies could host a larger fraction of the observed SNe. To test this hypothesis, we select CCSNe from the BTS and PTF samples that occur at offset of ≥ 15 kpc from massive ($\log(M[M_{\text{dot}}]) > 10$) galaxies. We manually examine the deepest publicly available survey data (if possible using the Legacy Survey or otherwise PS1 images) and exclude all cases where the SN occurred on or very close to pronounced structures that are part of the host galaxy, such as spiral arms extending to the SN location, or elevated ($> 3\sigma$) emission compared to the local background. We find the fraction of highly offset CCSNe occurring in elliptical compared to nonelliptical hosts is 0.33 (0.17–1.57; 95% confidence interval). This value is consistent with the fraction of massive ellipticals of all massive ($\log(M[M_{\odot}]) > 10$) galaxies in the Galaxy Zoo sample—0.33 (0.30–0.40; 95% confidence interval). To reduce the selection bias, we selected a low- z ($0.025 < z < 0.032$) sample such that the redshift distributions of elliptical galaxies, spiral galaxies, and all galaxies (including those with irregular or uncertain morphological classifications) match.

We conclude that the most likely explanation for the highly offset distribution of CCSNe near ellipticals is one of the following

1. a population of ultra-diffuse satellite star-forming galaxies near massive elliptical galaxies. The rate of highly offset CCSNe around massive ellipticals is hence similar to their rate around all massive galaxies. Due to the large number of CCSNe occurring in massive star-forming galaxies, the few offset events are unremarkable, but with very few events occurring in massive ellipticals, the offset population, perhaps arising from very faint satellites, stands out. Deeper observations of the location of our sample events are needed to establish this.
2. Some cases can be explained by extended and faint spiral features, or extended galaxy-scale star formation due to accretion of gas from the IGM. The latter would indicate inside-out growth of their elliptical host galaxies. Future

studies of the host galaxies of the CCSNe in our sample can also confirm or exclude this possibility.

5.4. The Star Formation Fraction in Elliptical Galaxies

We attempt to measure the formation rate of massive stars in elliptical galaxies through the fraction of CCSNe occurring in such environments in a fixed volume. The connection between the SFR and the CCSN rate has been previously established. Kennicutt (1984) found a linear correlation between the SFR and the CCSN rate, and used it to estimate a lower mass limit for the progenitor mass of CCSNe. Botticella et al. (2012) assume a lower mass limit of $8 M_{\odot}$ and derive a SFR for a complete sample of galaxies in the local universe. Their estimate agrees with the SFR implied from their FUV luminosities. Maoz et al. (2011) used a sample of 119 CCSNe from the Lick Observatory SN search (LOSS; Leaman et al. 2011; Li et al. 2011) and estimated a rate of 0.01 ± 0.002 SNe per M_{\odot} . If the CCSN rate per M_{\odot} is fixed across galaxy type, the fraction of CCSNe occurring in elliptical galaxies should reflect the fraction of the total star formation in their host galaxy population. Recently, Schulze et al. (2021) provided additional support for this claim by showing that the SN host-galaxy mass distributions are consistent with those of star-forming galaxies weighted by their star formation activity.

When measuring the fraction of CCSNe in elliptical galaxies, the different colors of elliptical and spiral galaxies could create a selection effect especially when considering galaxies with both UV–optical and MIR color information. Most notably, the redder UV–optical color of elliptical galaxies makes them less likely to have archival GALEX photometry compared to spirals at a similar optical brightness. However, our MIR photometry is not biased against ellipticals in the same way due to the brighter W2 magnitudes of massive ellipticals. W3 magnitudes distribute similarly for spirals and ellipticals. Figure 17 shows the magnitude distribution for the WISE/W2 band and GALEX/NUV band for all galaxies in the BTS Ia sample for elliptical and nonelliptical hosts. We illustrate that while ellipticals are less likely to be detected by GALEX at larger distances due to their faint NUV brightness, they are more likely to be detected by WISE. Thus, we derive estimates based on hosts with both UV–optical and MIR colors and based on hosts with MIR colors alone (using both definitions discussed in Section 2.1). A consistent result between both calculations will ensure that the selection effects in our samples are not strong. We also include a third estimate of the rate compared to

all CCSNe, regardless of their host-galaxy association. The resulting fractions are:

1. $R_{CC} = \frac{2}{478} = 0.4^{+0.5}_{-0.3}\%$ using both W2 – W3 and NUV-*r* color
2. $R_{CC} = \frac{3}{888} = 0.3^{+0.4}_{-0.1}\%$ based on our definition for ellipticals using only the W2 – W3 color and compared to all CCSNe associated with host galaxies.
3. $R_{CC} = \frac{3}{959} = 0.3^{+0.3}_{-0.1}\%$ based on our definition for ellipticals using only the W2 – W3 color, and compared to all CCSNe regardless of their host-galaxy association.

Statistical errors reflect the exact binomial 68% confidence interval on the reported values. We now compare the measured fraction of CCSNe in ellipticals ($\sim 0.4\%$) with the fraction of star formation ellipticals accounted for out of the total star formation produced by all galaxy types, calculated using the method of Cortese (2012) applied to UV and MIR observations.

We sum the total SFR of all Galaxy Zoo ellipticals which satisfy the color criteria in Section 2.1, and are within the range $0.025 < z < 0.032$, and compare it to the fraction of the total SFR in this redshift range in all galaxy types. We find that in this sample, the fraction of the total SFR produced by ellipticals is $1 \pm 0.01\%$, slightly higher ($\sim 2\sigma$) than the star formation inferred from the fraction of CCSNe in elliptical galaxies compared to all CCSNe. This could be explained due to additional UV emission by Active Galactic Nuclei (AGN) and old stellar populations (Jura 1982; Crocker et al. 2011), or due to an incomplete sample in the low-mass range of spiral galaxies (which host a significant fraction of CCSNe; Taggart & Perley 2021). Alternatively, this difference could reflect an underestimate of the SFR in spiral compared to elliptical galaxies due to the different total extinction of the host galaxies populations, or due to a different rate of failed SNe in both environments.

Our results are in significant tension with those of Kaviraj (2014), who claim that early-type galaxies (elliptical and lenticular) account for 14% of the star formation budget at $z < 0.07$. The sample in the study by Kaviraj (2014) is limited to bright < 16.8 mag galaxies, which account for 52% of the total star formation in our general Galaxy Zoo sample, but only for 5% of star formation in ellipticals. Thus ellipticals are over-represented in their sample.

Our findings highlight the importance of CCSN rates as independent tracers of SFR across a large range of sSFR and galaxy brightness, while preventing the severe selection effects associated with the low end of the galaxy brightness distribution. The planned Rubin Observatory Legacy Survey of Space and Time (LSST; Ivezić et al. 2019) is expected to increase the rate of CCSN detections by an order of magnitude in upcoming years. This will increase the number of CCSNe detected in elliptical hosts by an order-of-magnitude, allowing an in-depth study of the nature of star formation in and around elliptical hosts. However, we caution against using CCSNe as estimators of star formation without taking proper care to remove the significant contamination due to misclassified galaxies or SNe, or due to a false association of the SN with the host galaxy.

Della Valle et al. (2005) previously estimated elliptical galaxies might host up to 3% of CCSNe, based on a sample of SNe Ia in ellipticals from the Asiago SN survey (Cappellaro et al. 1999). Our findings place more stringent constraints on

the rate of CCSNe in ellipticals compared to those obtained in previous studies by an order of magnitude. Recently, Sedgwick et al. (2021) published a study of 36 CCSNe occurring in elliptical galaxies out of red photometrically classified CCSNe isolated from the SDSS-II survey at $z < 0.2$, suggesting that the fraction of CCSNe occurring in elliptical galaxies is significantly higher than the fraction we measure in this study ($\sim 8\%$ compared to our $\sim 0.4\%$). We point out that a population comprising of 8% of CCSNe would stand out in the spectroscopically complete BTS. Applying this rate to the 478 CCSN hosts with UV and MIR color information, we would expect to find 38 ± 6 CCSNe in elliptical galaxies, compared to the 2 found in our sample—a $> 5\sigma$ difference. We conclude that the fraction of CCSNe in ellipticals given by Sedgwick et al. (2021) is over estimated. This could be due to a contamination of their sample by misclassified SNe Ia. Sedgwick et al. (2021) define a confidently classified CCSN as having probability of $P_{Ia} < 0.05$ for being a SN Ia, based on their light curves alone. Since SNe Ia vastly outnumber CCSNe in elliptical hosts (in our sample, 240:2) the contamination of the CCSN sample due to falsely classified SNe Ia is likely significant, and could dominates their sample.

6. Summary and Conclusions

In this study, we conducted a systematic search for elliptical host galaxies of CCSNe in the ZTF BTS—a spectroscopically complete survey. In Section 2, we outlined the selection process for the candidates. We identified elliptical galaxies based on their UV–optical and MIR colors, or based on the MIR color alone. A control sample of morphologically classified galaxies confirms that we achieve a good separation between elliptical and spiral galaxies. We further visually verified that the morphology of the host galaxies is elliptical, with no disk or bar structures.

We identified three CCSNe that seem to be associated with elliptical galaxies. We presented their light curves, spectra, and host-galaxy photometry in Section 3, and analyzed our observations in Section 4. SN 2018fsh and SN 2020uik are spectroscopically regular SNe II which exploded in the outskirts of massive ellipticals with no signs of an alternative underlying host. SN 2020uik shows typical spectra for SNe II during its photospheric phase, while SN 2018fsh shows an extended and boxy H α profile in its nebular spectrum, a signature of CSM interaction. SN 2019ape is a SN Ic located in a massive elliptical near a compact star-forming region. Its *g*-band light curve shows a late-time second peak—a possible signature of extended CSM interaction, previously observed in other SNe Ic. Aside from this feature, a comparison to other SNe Ic shows it is a regular SN Ic and modeling a series of photospheric spectra reveals it had typical explosion properties. These, along with its location near a star formation site, point to a massive star origin.

We combine these objects with 7 literature CCSNe satisfying our criteria, and analyzed the properties of the combined sample of SNe and their host galaxies. We derived stellar masses and SFRs for the hosts and compared these to a control sample of SNe Ia in elliptical galaxies and BTS CCSNe. Our analysis concludes that elliptical galaxies hosting CCSNe are broadly consistent with the general population of ellipticals. We discussed the implications of our results in Section 5. We demonstrated that the peak *r*-band absolute magnitudes of SNe II in ellipticals are consistent with those of a sample of SNe II

from the BTS. We presented preliminary evidence that the offset distribution of CCSNe from their putative hosts extends to large offsets compared to both the BTS CCSN sample and a sample of SNe Ia in elliptical galaxies. However, this is not determined with high statistical significance, and verifying this requires a larger sample of events. We discussed possible reasons for the larger offset distribution and conclude that the most likely explanations are:

1. The CCSNe are hosted by a diffuse stellar population orbiting the nearby massive ellipticals. Since very few CCSNe occur in elliptical galaxies, a small population of CCSNe hosted by diffuse star-forming satellites would stand out. This is supported by the 1:3 ratio of highly offset CCSNe near spirals compared to elliptical galaxies—in agreement with ratio of massive spirals and ellipticals in the Galaxy Zoo sample.
2. The CCSNe originate from the nearby massive elliptical galaxy; either from faint peripheral spiral features, or due to extended galaxy-scale star formation due to gas accretion from the IGM.

Finally, we derived the fraction of CCSNe occurring in elliptical galaxies out of the general CCSN population and find it to be $0.4^{+0.5}_{-0.3}\%$ for SNe with a host galaxy associated with them, and $0.3^{+0.3}_{-0.1}\%$ when including hostless SNe. This is in slight tension ($\sim 2\sigma$) with the fraction of star formation in morphologically classified ellipticals satisfying the same color criteria and calculated using traditional tracers (found to be $1 \pm 0.01\%$). However, this might be explained by systematics in the calibration of SFR relations in elliptical galaxies due to UV emission from old stellar populations, or due to selection effects biasing the galaxy sample in the low end of the galaxy mass distribution. We conclude that CCSNe can be useful as direct tracers of star formation in low sSFR environments, but caution that proper care must be taken to avoid contamination of both the SN sample (by misclassified SNe Ia) and the host sample (by star-forming galaxies).

A.G.Y.'s research is supported by the EU via ERC grant No. 725161, the ISF GW excellence center, an IMOS space infrastructure grant, and BSF/Transformative and GIF grants, as well as The Benozio Endowment Fund for the Advancement of Science, the Deloro Institute for Advanced Research in Space and Optics, The Veronika A. Rabl Physics Discretionary Fund, Minerva, Yeda-Sela and the Schwartz/Reisman Collaborative Science Program; A.G.Y. is the incumbent of The Arlyn Imberman Professorial Chair. NLS is funded by the Deutsche Forschungsgemeinschaft (DFG, German Research Foundation) via the Walter Benjamin program 461903330. This research has made use of the NASA/IPAC Extragalactic Database (NED), which is operated by the Jet Propulsion Laboratory, California Institute of Technology, under contract with the National Aeronautics and Space Administration (NASA). Foscgui is a graphic user interface aimed at extracting SN spectroscopy and photometry obtained with FOSC-like instruments. It was developed by E. Cappellaro. A package description can be found at <http://sngroup.oapd.inaf.it/foscgui.html>. This work is based on observations obtained with the Samuel Oschin Telescope 48 inch and the 60 inch Telescope at the Palomar Observatory as part of the Zwicky Transient Facility project. ZTF is supported by the National Science Foundation under Grant

No. AST-1440341 and a collaboration including Caltech, IPAC, the Weizmann Institute for Science, the Oskar Klein Center at Stockholm University, the University of Maryland, the University of Washington, Deutsches Elektronen-Synchrotron and Humboldt University, Los Alamos National Laboratories, the TANGO Consortium of Taiwan, the University of Wisconsin at Milwaukee, and Lawrence Berkeley National Laboratories. Operations are conducted by COO, IPAC, and UW. Based on observations from the Las Cumbres Observatory network. The LCO team is supported by NSF grants AST-1911225 and AST-1911151 The Liverpool Telescope is operated on the island of La Palma by Liverpool John Moores University in the Spanish Observatorio del Roque de los Muchachos of the Instituto de Astrofísica de Canarias with financial support from the UK Science and Technology Facilities Council. Partly based on observations made with the Nordic Optical Telescope, operated at the Observatorio del Roque de los Muchachos, La Palma, Spain, of the Instituto de Astrofísica de Canarias. The SED Machine is based upon work supported by the National Science Foundation under grant No. 1106171. The ZTF forced-photometry service was funded under the Heising-Simons Foundation grant #12540303 (PI: Graham). The Legacy Surveys consist of three individual and complementary projects: the Dark Energy Camera Legacy Survey (DECaLS; Proposal ID #2014B-0404; PIs: David Schlegel and Arjun Dey), the Beijing-Arizona Sky Survey (BASS; NOAO Prop. ID #2015A-0801; PIs: Zhou Xu and Xiaohui Fan), and the Mayall z-band Legacy Survey (MzLS; Prop. ID #2016A-0453; PI: Arjun Dey). DECaLS, BASS and MzLS together include data obtained, respectively, at the Blanco telescope, Cerro Tololo Inter-American Observatory, NSF's NOIRLab; the Bok telescope, Steward Observatory, University of Arizona; and the Mayall telescope, Kitt Peak National Observatory, NOIRLab. The Legacy Surveys project is honored to be permitted to conduct astronomical research on Iolkam Du'ag (Kitt Peak), a mountain with particular significance to the Tohono O'odham Nation. BASS is a key project of the Telescope Access Program (TAP), which has been funded by the National Astronomical Observatories of China, the Chinese Academy of Sciences (the Strategic Priority Research Program The Emergence of Cosmological Structures Grant # XDB09000000), and the Special Fund for Astronomy from the Ministry of Finance. The BASS is also supported by the External Cooperation Program of Chinese Academy of Sciences (Grant # 114A11KYSB20160057), and Chinese National Natural Science Foundation (Grant # 11433005) This project has made use of data products from the Near-Earth Object Wide-field Infrared Survey Explorer (NEOWISE), which is a project of the Jet Propulsion Laboratory/California Institute of Technology. NEOWISE is funded by the National Aeronautics and Space Administration. Based on observations collected at the European Organisation for Astronomical Research in the Southern Hemisphere, Chile, as part of ePESSTO/ePESSTO+ (the extended Public ESO Spectroscopic Survey for Transient Objects Survey) under ESO programmes 199.D-0143,1103.D-0328,106.216C.001/007,106.216C.002/008& 106.216C.003/009. This research has made use of the VizieR catalog access tool, CDS, Strasbourg, France (DOI:10.26093/cds/vizieR). The original description of the VizieR service was published in 2000, A&AS 143, 23 This work has made use of

data from the Asteroid Terrestrial-impact Last Alert System (ATLAS) project. ATLAS is primarily funded to search for near Earth asteroids through NASA grants NN12AR55G, 80NSSC18K0284, and 80NSSC18K1575; by products of the NEO search include images and catalogs from the survey area. The ATLAS science products have been made possible through the contributions of the University of Hawaii Institute for Astronomy, the Queen's University Belfast, and the Space Telescope Science Institute. TMB was funded by the CONICYT PFCHA/DOCTORADOBECAS CHILE/2017-72180113. MN is supported by a Royal Astronomical Society Research Fellowship and by the European Research Council (ERC) under the European Union's Horizon 2020 research and innovation program (grant agreement No. 948381 M.M. K. acknowledges generous support from the David and Lucille Packard Foundation. This work was supported by the GROWTH Marshal (Kasliwal et al. 2019) developed as part of the GROWTH (Global Relay of Observatories Watching Transients Happen) project funded by the National Science Foundation under grant No. 1545949. M.G. is supported by the EU Horizon 2020 research and innovation program under grant agreement No 101004719. L.G. acknowledges financial support from the Spanish Ministry of Science, Innovation and Universities (MICIU) under the 2019 Ramón y Cajal program RYC2019-027683 and from the Spanish MICIU project PID2020-115253GA-I00. T.-W.C. acknowledges the EU Funding under Marie Skłodowska-Curie grant H2020-MSCA-IF-2018-842471. E.C.K. acknowledges support from the G.R.E.A.T research environment funded by *Vetenskapsrådet*, the Swedish Research Council, under project number 2016-06012, and support from The Wenner-Gren Foundations. L.G. acknowledges financial support from the Spanish Ministry of Science, Innovation and Universities (MICIU) under the 2019 Ramón y Cajal program RYC2019-027683 and from the Spanish MICIU project PID2020-115253GA-I00.

ORCID iDs

I. Irani  <https://orcid.org/0000-0002-7996-8780>
 S. J. Prentice  <https://orcid.org/0000-0003-0486-6242>
 S. Schulze  <https://orcid.org/0000-0001-6797-1889>
 A. Gal-Yam  <https://orcid.org/0000-0002-3653-5598>
 Paolo Mazzali  <https://orcid.org/0000-0001-6876-8284>
 J. Sollerman  <https://orcid.org/0000-0003-1546-6615>
 K. Taggart  <https://orcid.org/0000-0002-5748-4558>
 Kishalay De  <https://orcid.org/0000-0002-8989-0542>
 Christoffer Fremling  <https://orcid.org/0000-0002-4223-103X>
 Daniel A. Perley  <https://orcid.org/0000-0001-8472-1996>
 Nora L. Strotjohann  <https://orcid.org/0000-0002-4667-6730>
 Mansi M. Kasliwal  <https://orcid.org/0000-0002-5619-4938>
 S. Dhawan  <https://orcid.org/0000-0002-2376-6979>
 Anastasios Tzanidakis  <https://orcid.org/0000-0003-0484-3331>
 Daichi Hiramatsu  <https://orcid.org/0000-0002-1125-9187>
 Erik C. Kool  <https://orcid.org/0000-0002-7252-3877>
 J. P. Anderson  <https://orcid.org/0000-0003-0227-3451>
 T. E. Müller-Bravo  <https://orcid.org/0000-0003-3939-7167>
 Richard Dekany  <https://orcid.org/0000-0002-5884-7867>
 Mariusz Gromadzki  <https://orcid.org/0000-0002-1650-1518>
 Roberta Carini  <https://orcid.org/0000-0003-1604-2064>
 L. Galbany  <https://orcid.org/0000-0002-1296-6887>

Jamison Burke  <https://orcid.org/0000-0003-0035-6659>
 Craig Pellegrino  <https://orcid.org/0000-0002-7472-1279>
 Massimo Della Valle  <https://orcid.org/0000-0003-3142-5020>
 Michael S. Medford  <https://orcid.org/0000-0002-7226-0659>
 Ben Rusholme  <https://orcid.org/0000-0001-7648-4142>
 D. R. Young  <https://orcid.org/0000-0002-1229-2499>
 Claudia P. Gutiérrez  <https://orcid.org/0000-0003-2375-2064>
 Cosimo Inserra  <https://orcid.org/0000-0002-3968-4409>
 David L. Shupe  <https://orcid.org/0000-0003-4401-0430>
 Kyung Min Shin  <https://orcid.org/0000-0002-1486-3582>
 Ofer Yaron  <https://orcid.org/0000-0002-0301-8017>
 Curtis McCully  <https://orcid.org/0000-0001-5807-7893>
 Matt Nicholl  <https://orcid.org/0000-0002-2555-3192>
 Reed Riddle  <https://orcid.org/0000-0002-0387-370X>

References

- Abbott, D. C., & Lucy, L. B. 1985, *ApJ*, **288**, 679
 Ahn, C. P., Alexandroff, R., Allende Prieto, C., et al. 2012, *ApJS*, **203**, 21
 Alam, S., Albareti, F. D., Allende Prieto, C., et al. 2015, *ApJS*, **219**, 12
 Anderson, J. P., James, P. A., Habergham, S. M., Galbany, L., & Kuncarayakti, H. 2015, *PASA*, **32**, e019
 Arcavi, I. 2017, in *Handbook of Supernovae*, ed. A. W. Alsabti & P. Murdin (AG: Springer International Publishing), 239
 Armstrong, M. 2003, *IAU Circ.*, **8254**, 1
 Ashall, C., & Mazzali, P. A. 2020, *MNRAS*, **492**, 5956
 Ashall, C., Mazzali, P. A., Pian, E., et al. 2019, *MNRAS*, **487**, 5824
 Bellm, E. C., & Sesar, B. 2016, *pyraf-dbsp: Reduction Pipeline for the Palomar Double Beam Spectrograph*, Astrophysics Source Code Library, [ascl:1602.002](https://ui.adsabs.org/abs/2016ASCl..1602002)
 Bellm, E. C., Kulkarni, S. R., Graham, M. J., et al. 2019, *PASP*, **131**, 018002
 Ben-Ami, S., Gal-Yam, A., Mazzali, P. A., et al. 2014, *ApJ*, **785**, 37
 Bertin, E., Mellier, Y., Radovich, M., et al. 2002, in *ASP Conf. Ser.*, 281, *Astronomical Data Analysis Software and Systems XI*, ed. D. A. Bohlender, D. Durand, & T. H. Handley (San Francisco, CA: ASP), 228
 Blagorodnova, N., Neill, J. D., Walters, R., et al. 2018, *PASP*, **130**, 035003
 Blondin, S., & Tonry, J. L. 2007, *ApJ*, **666**, 1024
 Botticella, M. T., Smartt, S. J., Kennicutt, R. C., et al. 2012, *A&A*, **537**, A132
 Bourne, N., Maddox, S. J., Dunne, L., et al. 2012, *MNRAS*, **421**, 3027
 Buat, V., Donas, J., Milliard, B., & Xu, C. 1999, *A&A*, **352**, 371
 Buta, R. J. 2011, *arXiv:1102.0550*
 Buzzoni, B., Delabre, B., Dekker, H., et al. 1984, *Msngr*, **38**, 9
 Calzetti, D., Bohlin, R. C., Kinney, A. L., Storchi-Bergmann, T., & Heckman, T. M. 1995, *ApJ*, **443**, 136
 Cappellaro, E., Evans, R., & Turatto, M. 1999, *A&A*, **351**, 459
 Carini, R., Palazzi, E., Cappellaro, E., Fiore, A., & Yaron, O. 2019, *Transient Name Server Classification Report No. 2019-220*
 Cenko, S. B., Fox, D. B., Moon, D.-S., et al. 2006, *PASP*, **118**, 1396
 Chambers, K. C., Huber, M. E., Flewelling, H., et al. 2019, *Transient Name Server Discovery Report No. 2019-5*
 Chambers, K. C., Magnier, E. A., Metcalfe, N., et al. 2016, *arXiv:1612.05560*
 Cortese, L. 2012, *A&A*, **543**, A132
 Crocker, A. F., Bureau, M., Young, L. M., & Combes, F. 2011, *MNRAS*, **410**, 1197
 Cutri, R. M., Wright, E. L., Conrow, T., et al. 2021, *VizieR On-line Data Catalog: II/328*
 Dahiwal, A., & Fremling, C. 2020, *Transient Name Server Classification Report No. 2020-2020*
 De, K., Kasliwal, M. M., Tzanidakis, A., et al. 2020, *ApJ*, **905**, 58
 De Lucia, G., Springel, V., White, S. D. M., Croton, D., & Kauffmann, G. 2006, *MNRAS*, **366**, 499
 de Vaucouleurs, G. 1959, *HDP*, **53**, 275
 de Jaeger, T., Zheng, W., Stahl, B. E., et al. 2019, *MNRAS*, **490**, 2799
 Dekany, R., Smith, R. M., Riddle, R., et al. 2020, *PASP*, **132**, 038001
 Della Valle, M., Panagia, N., Padovani, P., et al. 2005, *ApJ*, **629**, 750
 Dey, A., Schlegel, D. J., Lang, D., et al. 2019, *AJ*, **157**, 168
 Drout, M. R., Soderberg, A. M., Gal-Yam, A., et al. 2011, *ApJ*, **741**, 97

- Eldridge, J. J., Fraser, M., Smartt, S. J., Maund, J. R., & Crockett, R. M. 2013, *MNRAS*, **436**, 774
- Filippenko, A. V., Barth, A. J., Matheson, T., et al. 1995, *ApJL*, **450**, L11
- Filippenko, A. V., Matheson, T., & Barth, A. J. 1994, *AJ*, **108**, 2220
- Flewelling, H. A., Magnier, E. A., Chambers, K. C., et al. 2020, *ApJS*, **251**, 7
- Foley, R. J. 2015, *MNRAS*, **452**, 2463
- Fremming, C. 2018, Transient Name Server Discovery Report No. 2018-543
- Fremming, C., Miller, A. A., Sharma, Y., et al. 2020, *ApJ*, **895**, 32
- Fremming, C., Sharma, Y., & Dugas, A. 2018, Transient Name Server Classification Report No. 2018-2048
- Fremming, C., Sollerman, J., Taddia, F., et al. 2016, *A&A*, **593**, A68
- Frohmaier, C., Sullivan, M., Nugent, P. E., Goldstein, D. A., & DeRose, J. 2017, *ApJS*, **230**, 4
- Gabor, J. M., Davé, R., Finlator, K., & Oppenheimer, B. D. 2010, *MNRAS*, **407**, 749
- Gal-Yam, A. 2017, in Handbook of Supernovae, ed. A. W. Alsabti & P. Murdin (New York: Springer International), 195
- Gal-Yam, A., Maoz, D., Guhathakurta, P., & Filippenko, A. V. 2003, *AJ*, **125**, 1087
- Ginsburg, A., Sipőcz, B. M., Brasseur, C. E., et al. 2019, *AJ*, **157**, 98
- Gomes, J. M., Papaderos, P., Vílchez, J. M., et al. 2016, *A&A*, **585**, A92
- Graham, M. J., Kulkarni, S. R., Bellm, E. C., et al. 2019, *PASP*, **131**, 078001
- Graham, M. L., Sand, D. J., Bildfell, C. J., et al. 2012, *ApJ*, **753**, 68
- Guillochon, J., Parrent, J., Kelley, L. Z., & Margutti, R. 2017, *ApJ*, **835**, 64
- Gutiérrez, C. P., Bersten, M. C., Orellana, M., et al. 2021, *MNRAS*, **504**, 4907
- Hachinger, S., Mazzali, P. A., Taubenberger, S., Pakmor, R., & Hillebrandt, W. 2009, *MNRAS*, **399**, 1238
- Hakobyan, A. A., Adibekyan, V. Z., Aramyan, L. S., et al. 2012, *A&A*, **544**, A81
- Hakobyan, A. A., Petrosian, A. R., McLean, B., et al. 2008, *A&A*, **488**, 523
- Hernández, F. C., & Bruzual, G. 2009, *RMxAA*, **35**, 158
- Hosseinzadeh, G., McCully, C., Zabludoff, A. I., et al. 2019, *ApJ*, **871**, L9
- Howell, D. 2019, AAS Meeting, **233**, 258.16
- Howell, D. A., Sullivan, M., Perrett, K., et al. 2005, *ApJ*, **634**, 1190
- Hubble, E. P. 1926, *ApJ*, **64**, 321
- Irani, I., Schulze, S., Gal-Yam, A., et al. 2019, *ApJ*, **887**, 127
- Ivezić, Ž., Kahn, S. M., Tyson, J. A., et al. 2019, *ApJ*, **873**, 111
- Jerkstrand, A., Ergon, M., Smartt, S. J., et al. 2015, *A&A*, **573**, A12
- Jerkstrand, A., Maeda, K., & Kawabata, K. S. 2020, *Sci*, **367**, 415
- Joye, W. A., & Mandel, E. 2003, in ASP Conf. Ser., **295**, Astronomical Data Analysis Software and Systems XII, ed. H. E. Payne, R. I. Jedrzejewski, & R. N. Hook (San Francisco, CA: ASP), 489
- Jura, M. 1982, *ApJ*, **254**, 70
- Kasliwal, M. M., Cannella, C., Bagdasaryan, A., et al. 2019, *PASP*, **131**, 038003
- Kasliwal, M. M., Kulkarni, S. R., Gal-Yam, A., et al. 2012, *ApJ*, **755**, 161
- Kaviraj, S. 2014, *MNRAS*, **437**, L41
- Kaviraj, S., Khochfar, S., Schawinski, K., et al. 2008, *MNRAS*, **388**, 67
- Kennicutt, R. C. J. 1984, *ApJ*, **277**, 361
- Kennicutt, R. C. J., Edgar, B. K., & Hodge, P. W. 1989, *ApJ*, **337**, 761
- Kennicutt, R. C., Jr. 1998, *ARA&A*, **36**, 189
- Kulkarni, S. R. 2013, *ATel*, **4807**, 1
- Lang, D. 2014, *AJ*, **147**, 108
- Law, N. M., Kulkarni, S. R., Dekany, R. G., et al. 2009, *PASP*, **121**, 1395
- Leaman, J., Li, W., Chornock, R., & Filippenko, A. V. 2011, *MNRAS*, **412**, 1419
- Lee, G.-H., Hwang, H. S., Sohn, J., & Lee, M. G. 2017, *ApJ*, **835**, 280
- Li, W., Leaman, J., Chornock, R., et al. 2011, *MNRAS*, **412**, 1441
- Lintott, C., Schawinski, K., Bamford, S., et al. 2011, *MNRAS*, **410**, 166
- Lucy, L. B. 1999, *A&A*, **345**, 211
- Lunnan, R., Kasliwal, M. M., Cao, Y., et al. 2017, *ApJ*, **836**, 60
- Lupton, R., Blanton, M. R., Fekete, G., et al. 2004, *PASP*, **116**, 133
- Man, A., & Belli, S. 2018, *NatAs*, **2**, 695
- Maoz, D., Mannucci, F., Li, W., et al. 2011, *MNRAS*, **412**, 1508
- Martin, D. C., Fanson, J., Schiminovich, D., et al. 2005, *ApJL*, **619**, L1
- Masci, F. J., Laher, R. R., Rusholme, B., et al. 2018, *PASP*, **131**, 018003
- Mazzali, P. A. 2000, *A&A*, **363**, 705
- Mazzali, P. A., Deng, J., Maeda, K., et al. 2002, *ApJL*, **572**, L61
- Mazzali, P. A., Deng, J., Nomoto, K., et al. 2006, *Natur*, **442**, 1018
- Mazzali, P. A., Iwamoto, K., & Nomoto, K. 2000, *ApJ*, **545**, 407
- Mazzali, P. A., & Lucy, L. B. 1993, *A&A*, **279**, 447
- Mazzali, P. A., Sauer, D. N., Pian, E., et al. 2017, *MNRAS*, **469**, 2498
- Meisner, A. M., Lang, D., & Schlegel, D. J. 2017, *AJ*, **153**, 38
- Modjaz, M., Blondin, S., Kirshner, R. P., et al. 2014, *AJ*, **147**, 99
- Mould, J. R., Huchra, J. P., Freedman, W. L., et al. 2000, *ApJ*, **529**, 786
- Mowla, L., van der Wel, A., van Dokkum, P., & Miller, T. B. 2019, *ApJL*, **872**, L13
- Nomoto, K., Yamaoka, H., Pols, O. R., et al. 1994, *Natur*, **371**, 227
- Ochsenbein, F., Bauer, P., & Marcout, J. 2000, *A&AS*, **143**, 23
- Ofeek, E. O., Cameron, P. B., Kasliwal, M. M., et al. 2007, *ApJL*, **659**, L13
- Oke, J. B., & Gunn, J. E. 1982, *PASP*, **94**, 586
- Oke, J. B., Cohen, J. G., Carr, M., et al. 1995, *PASP*, **107**, 375
- OMullane, W., Li, N., Nieto-Santisteban, M., et al. 2005, arXiv:cs/0502072
- Patat, F., Chugai, N., & Mazzali, P. A. 1995, *A&A*, **299**, 715
- Paudrach, A. W. A., Duschinger, M., Mazzali, P. A., et al. 1996, *A&A*, **312**, 525
- Perets, H. B., Gal-Yam, A., Mazzali, P. A., et al. 2010, *Natur*, **465**, 322
- Pérez, E., Cid Fernandes, R., González Delgado, R. M., et al. 2013, *ApJL*, **764**, L1
- Perley, D. A. 2019, *PASP*, **131**, 084503
- Perley, D. A., Fremming, C., Sollerman, J., et al. 2020, *ApJ*, **904**, 35
- Perley, D. A., Quimby, R. M., Yan, L., et al. 2016, *ApJ*, **830**, 13
- Petty, S. M., Neill, J. D., Jarrett, T. H., et al. 2013, *AJ*, **146**, 77
- Piascik, A. S., Steele, I. A., Bates, S. D., et al. 2014, *Proc. SPIE*, **9147**, 91478H
- Poznanski, D., Prochaska, J. X., & Bloom, J. S. 2012, *MNRAS*, **426**, 1465
- Pozzo, M., Meikle, W. P. S., Fassia, A., et al. 2004, *MNRAS*, **352**, 457
- Prentice, S. J., Ashall, C., James, P. A., et al. 2018a, *MNRAS*, **485**, 1559
- Prentice, S. J., Ashall, C., Mazzali, P. A., et al. 2018b, *MNRAS*, **478**, 4162
- Prentice, S. J., & Mazzali, P. A. 2017, *MNRAS*, **469**, 2672
- Prentice, S. J., Mazzali, P. A., Pian, E., et al. 2016, *MNRAS*, **458**, 2973
- Puckett, T., Peoples, M., Joubert, N., et al. 2006, *IAU Circ.*, **8741**, 1
- Rigault, M., Neill, J. D., Blagorodnova, N., et al. 2019, *A&A*, **627**, A115
- Ruiz, P., Trujillo, I., & Mármol-Queraltó, E. 2014, *MNRAS*, **442**, 347
- Sako, M., Bassett, B., Becker, A. C., et al. 2018, *PASP*, **130**, 064002
- Salim, S., Fang, J. J., Rich, R. M., Faber, S. M., & Thilker, D. A. 2012, *ApJ*, **755**, 105
- Salim, S., Rich, R. M., Charlot, S., et al. 2007, *ApJS*, **173**, 267
- Sánchez-Blázquez, P., Forbes, D. A., Strader, J., Brodie, J., & Proctor, R. 2007, *MNRAS*, **377**, 759
- Sandage, A. 1961, The Hubble Atlas of Galaxies (Washington, DC: Carnegie Institution)
- Sanders, N. E., Soderberg, A. M., Foley, R. J., et al. 2013, *ApJ*, **769**, 39
- Sauer, D. N., Mazzali, P. A., Deng, J., et al. 2006, *MNRAS*, **369**, 1939
- Schlafly, E. F., & Finkbeiner, D. P. 2011, *ApJ*, **737**, 103
- Schulze, S., Krühler, T., Leloudas, G., et al. 2018, *MNRAS*, **473**, 1258
- Schulze, S., Yaron, O., Sollerman, J., et al. 2021, *ApJS*, **255**, 29
- Sedgwick, T. M., Baldry, I. K., James, P. A., Kaviraj, S., & Martin, G. 2021, arXiv:2106.13812
- Sedgwick, T. M., Baldry, I. K., James, P. A., & Kelvin, L. S. 2019, *MNRAS*, **484**, 5278
- Shappee, B., Prieto, J., Stanek, K. Z., et al. 2014, AAS Meeting, **223**, 236.03
- Skrutskie, M. F., Cutri, R. M., Stiening, R., et al. 2006, *AJ*, **131**, 1163
- Smartt, S. J. 2015, *PASA*, **32**, e016
- Smartt, S. J., Valenti, S., Fraser, M., et al. 2015, *A&A*, **579**, A40
- Smith, K. W., Smartt, S. J., Young, D. R., et al. 2020, *PASP*, **132**, 085002
- Smith, N., Li, W., Foley, R. J., et al. 2007, *ApJ*, **666**, 1116
- Smith, R. J., Piascik, A. S., Steele, I. A., & Barnsley, R. M. 2016, *Proc. SPIE*, **9913**, 991317
- Soker, N. 2019, *SCPMA*, **62**, 119501
- Sollerman, J., Yang, S., Schulze, S., et al. 2021, arXiv:2107.14503
- Spergel, D. N., Bean, R., Doré, O., et al. 2007, *ApJS*, **170**, 377
- Steele, I. A., Smith, R. J., Rees, P. C., et al. 2004, *Proc. SPIE*, **5489**, 679
- Stratova, I., Ivezić, Ž., Knapp, G. R., et al. 2001, *AJ*, **122**, 1861
- Stritzinger, M. D., Taddia, F., Burns, C. R., et al. 2018, *A&A*, **609**, A135
- Suh, H., Yoon, S.-c., Jeong, H., & Yi, S. K. 2011, *ApJ*, **730**, 110
- Taddia, F., Sollerman, J., Fremming, C., et al. 2019, *A&A*, **621**, A71
- Taggart, K., & Perley, D. A. 2021, *MNRAS*, **503**, 3931
- Taubenberger, S., Pastorello, A., Mazzali, P. A., et al. 2006, *MNRAS*, **371**, 1459
- Teffs, J. J., Prentice, S. J., Mazzali, P. A., & Ashall, C. 2021, *MNRAS*, **502**, 3829
- Tony, J., Denneau, L., Heinze, A., et al. 2020, Transient Name Server Discovery Report No. 2020-2
- Tony, J. L., Denneau, L., Heinze, A. N., et al. 2018, *PASP*, **130**, 064505
- Trager, S. C., Faber, S. M., Worthey, G., & González, J. J. 2000, *AJ*, **120**, 165
- Trujillo, I., Roman, J., Filho, M., & Almeida, J. S. 2017, *ApJ*, **836**, 191
- Valenti, S., Elias-Rosa, N., Taubenberger, S., et al. 2008, *ApJL*, **673**, L155
- Van Dyk, S. D. 2017, *RSPTA*, **375**, 20160277
- Van Dyk, S. D., Zheng, W., Brink, T. G., et al. 2018, *ApJ*, **860**, 90
- Wen, X.-Q., Wu, H., Zhu, Y.-N., et al. 2013, *MNRAS*, **433**, 2946
- Woolsey, S. E., Pinto, P. A., & Hartmann, D. 1989, *ApJ*, **346**, 395

Wright, A. H., Robotham, A. S. G., Bourne, N., et al. 2016, [MNRAS](#), **460**, 765
Yaron, O., & Gal-Yam, A. 2012, [PASP](#), **124**, 668
Yaron, O., Perley, D. A., Gal-Yam, A., et al. 2017, [NatPh](#), **13**, 510
Yi, S. K., Yoon, S.-J., Kaviraj, S., et al. 2005, [ApJ](#), **619**, L111

York, D. G., Adelman, J., Anderson, J. E., Jr., et al. 2000, [AJ](#), **120**, 1579
Zackay, B., Ofek, E. O., & Gal-Yam, A. 2016, [ApJ](#), **830**, 27
Zapartas, E., de Mink, S. E., Izzard, R. G., et al. 2017, [A&A](#), **601**, A29
Zou, H., Zhou, X., Fan, X., et al. 2017, [PASP](#), **129**, 064101